Since January 2020 Elsevier has created a COVID-19 resource centre with free information in English and Mandarin on the novel coronavirus COVID-19. The COVID-19 resource centre is hosted on Elsevier Connect, the company's public news and information website.

Journal of Molecular Structure 1250 (2022) 131782

Contents lists available at ScienceDirect

Journal of Molecular Structure

journal homepage: www.elsevier.com/locate/molstr

Design and synthesis of heterocyclic azole based bioactive compounds: Molecular structures, quantum simulation, and mechanistic studies through docking as multi-target inhibitors of SARS-CoV-2 and cytotoxicity

Jebiti Haribabu[a,b], Vasavi Garisetti[c], Rahime Eshaghi Malekshah[d,e], Swaminathan Srividya[a], Dasararaju Gayathri[c], Nattamai Bhuvanesh[f], Ramalinga Viswanathan Mangalaraja[g], Cesar Echeverria[b,*], Ramasamy Karvembu[a,*]

[a] Department of Chemistry, National Institute of Technology, Tiruchirappalli 620015, India
[b] Facultad de Medicina, Universidad de Atacama, Los Carreras 1579, 1532502 Copiapo, Chile
[c] Centre of Advanced Study in Crystallography and Biophysics, University of Madras, Guindy Campus, Chennai 600025, India
[d] Medical Biomaterial Research Centre (MBRC), Tehran University of Medical Sciences, Tehran, Iran
[e] Department of Chemistry, Iran University of Science and Technology, Tehran 16846–13114, Iran
[f] Department of Chemistry, Texas A & M University, College Station, TX 77842, USA
[g] Advanced Ceramics and Nanotechnology Laboratory, Department of Materials Engineering, Faculty of Engineering, University of Concepcion, Concepcion, Chile

ARTICLE INFO

Article history:
Received 30 July 2021
Revised 16 October 2021
Accepted 19 October 2021
Available online 21 October 2021

Keywords:
Heterocyclic azoles
Multi-target inhibitors
SARS-CoV-2
Quantum simulation
Molecular docking
Cytotoxicity

ABSTRACT

Two heterocyclic azole compounds, 3-(2,3-dihydrobenzo[d]thiazol-2-yl)-4H-chromen-4-one (**SVS1**) and 5-(1H-indol-3-yl)-4-methyl-2,4-dihydro-3H-1,2,4-triazole-3-thione (**SVS2**) were obtained unexpectedly from 2-aminothiophenol and 4-oxo-4H-chromene-3-carbaldehyde (for **SVS1**), and (*E*)-2-((1H-indol-3-yl)methylene)-N-methylhydrazine-1-carbothioamide in the presence of anhydrous $FeCl_3$ (for **SVS2**), respectively. The compounds were well characterized by analytical and spectroscopic tools. The molecular structures of both the compounds were determined by single crystal X-ray diffraction (XRD) study. The results obtained from density functional theory (DFT) study revealed the molecular geometry and electron distribution of the compounds, which were correlated well with the three-dimensional structures obtained from the single crystal XRD. DMol^3 was used to calculate quantum chemical parameters [chemical potential (μ), global hardness (η), global softness (σ), absolute electronegativity (χ) and electrophilicity index (ω)] of **SVS1** and **SVS2**. Molecular docking study was performed to elucidate the binding ability of **SVS1** and **SVS2** with SARS-CoV-2 main protease and human angiotensin-converting enzyme-2 (ACE-2) molecular targets. Interestingly, the binding efficiency of the compounds with the molecular targets was comparable with that of remdesivir (SARS-CoV-2), chloroquine and hydroxychloroquine. **SVS1** showed better docking energy than **SVS2**. The molecular docking study was complemented by molecular dynamics simulation study of SARS-CoV-2 main protease-**SVS1** complex, which further exemplified the binding ability of **SVS1** with the target. In addition, **SVS1, SVS2** and cisplatin were assessed for their cytotoxicity against a panel of three human cancer cells such as HepG-2 (hepatic carcinoma), T24 (bladder) and EA.hy926 (endothelial), as well as Vero (kidney epithelial cells extracted from an African green monkey) normal cells using MTT assay. The results showed that **SVS2** has significant cytotoxicity against HepG-2 and EA.hy926 cells with the IC_{50} values of 33.8 μM (IC_{50} = 49.9 μM-cisplatin and 8.6 μM-doxorubicin) and 29.2 (IC_{50} = 26.6 μM-cisplatin and 3.8 μM-doxorubicin), respectively.

1. Introduction

Outbreak of SARS-CoV-2 (severe acute respiratory syndrome coronavirus-2) has led to more than 100 million cases and 2 million deaths as reported by WHO (World Health Organization), and

* Corresponding authors.
E-mail addresses: cesar.echeverria@uda.cl (C. Echeverria), kar@nitt.edu (R. Karvembu).

https://doi.org/10.1016/j.molstruc.2021.131782
0022-2860/

these numbers are still counting. Due to this universal life threat to humans, a global response to prepare health systems is a priority [1].

Four types of CoVs namely α, β, γ and δ were identified. Among the four, γ and δ are known to affect birds, whereas α and β affect mammals [2,3]. The novel SARS-CoV-2 belongs to β-coronavirus lineage with four main proteins, namely, spike (S) protein (binds with bronchial epithelial cells and type-II pneumocytes after entering the host cells with the help of ACE-2 and TMPRSS2 receptors through endocytosis), membrane (M) protein (acts as an organizer of CoV assembly), envelope (E) protein (interacts with membrane protein to form an envelope) and nucleocapsid (N) protein (viral RNA genome replication) [2]. Some nucleotide analogous drugs like remdesivir and galidesivir interrupt the process of viral replication by interacting with RNA-dependent RNA polymerase (RdRp), an enzyme that plays a vital role in virus replication. Some studies demonstrated that chloroquine (CQ) and hydroxychloroquine (HCQ) can reasonably inhibit SARS-CoV-2. CQ and HCQ are also suggested to block the virus entry through glycosylation of host ACE-2 receptor. Remdesivir showed inhibition activity against a variety of non-structural proteins such as RdRp [4,5].

To date, due to its high toxicity and the virus resistance to the drug, no effective dedicated treatments are approved for treating such CoVs. The development of new therapeutic anticorona agents made so far has also been limited [4,5]. Heterocyclic compounds such as triazole, thiazole, pyrrole, pyridine, quinolone, *etc.*, and their derivatives are characterized as important classes of organic compounds that exhibit various biological and medicinal properties such as antitumor [6,7], EGFR inhibitory [8], antioxidant [9,10], antianalgesic, antiinflammatory [11], antibacterial [12], antifungal [13], antimicrobial [14], *etc*. The biological properties of many nitrogen based heterocyclic compounds such as triazole and its derivatives have been investigated [15]. Detailed studies have shown that they possess significant biological properties [16–18]. Demirbas et al., reported the antimicrobial activities of the triazole derivatives against several bacterial and yeast strains. The results showed that triazole derivatives are one of the active components to increase the antimicrobial activities [19]. In addition, a series of 1,2,4-triazole compounds showed significant antitumoral activity, and acetylcholinesterase (AChE) and human carbonic anhydrase enzymes inhibition [20]. The compounds including indole and their analogs were evaluated for their anti-hepatitis B virus (HBV), anti-inflammatory, antifungal activities, and the treatment of acute lung injury [21–24], *etc*. Chromones and their derivatives have played a vital role in the human diet. Many biologically active compounds derived from natural sources comprise of chromone moiety as their core [25–27]. These compounds have attracted the pharmaceutical industries to a large extent owing to their antioxidant, antitumor and antibacterial activities [28–30]. Besides these, several chromone derivatives have been used as antimicrobial, DNA binding, DNA cleavage, anticancer, anti-allergic, neuroprotective and pesticidal agents [31–33].

Due to the existence of chromone- and heterocyclic azole-based structures in many drugs, we were motivated to synthesize such heterocyclic compounds for biological applications. In this connection, we report the synthesis of two heterocyclic compounds (**SVS1** and **SVS2**), and the main objectives of the study are to solve the three-dimensional structures, and to explore the various pharmaceutical potentials of the compounds through *in silico* and *in vitro* studies. The compounds were characterized by single crystal XRD, and FT-IR, UV-Visible, ^{1}H NMR and ^{13}C NMR spectroscopy. The quantum chemical parameters of the compounds were calculated by using Materials Studio 2017. Molecular docking studies were carried out to know their interactions with the main protease of SARS-CoV-2 and human ACE-2 receptors. The molecular docking results were further supported by molecular dynamics simulation studies. The cytotoxic potential of **SVS1** and **SVS2** along with the standard drugs (cisplatin and doxorubicin) was assessed using MTT assay against three cancer (HepG-2, T24 and EA.hy926) and one normal (Vero) cell lines.

2. Experimental

2.1. Materials and methods

Chromone-3-carboxaldehyde, 2-aminothiophenol, anhydrous $FeCl_3$ and solvents were purchased from commercial suppliers (Sigma Aldrich or Alfa Aesar) and used as received. (*E*)-2-((1H-indol-3-yl)methylene)-N-methylhydrazine-1-carbothioamide was prepared according to the previously reported procedure by us [34–36]. The melting points were measured on a Lab India instrument and are uncorrected. CHNS analyses were carried out using a Vario EL III CHNS instrument. FT-IR spectra were obtained as KBr pellets using a Ncolet-iS5 spectrophotometer. UV-Visible spectra were recorded using a Shimadzu-2600 spectrophotometer. NMR spectra were recorded in DMSO–d_6/$CDCl_3$ solvent using TMS as an internal standard on a Bruker 500 MHz spectrometer.

2.2. Synthesis

2.2.1. Synthesis of 3-(2,3-dihydrobenzo[d]thiazol-2-yl)-4H-chromen-4-one (*SVS1*)

The compound was synthesized by mixing an equimolar amount of 4-oxo-4H-chromene-3-carbaldehyde (174 mg, 1 mmol) with 2-aminothiophenol (125 mg, 1 mmol) in 10 mL of ethanol, and the reaction mixture was refluxed for 4 h. The yellow color solid was filtered off from the reaction mixture, washed with cold ethanol and diethyl ether, and then dried at room temperature. The yellow block crystals of **SVS1** suitable for single crystal XRD were obtained by slow evaporation of the compound in chloroform and dimethylformamide mixture (8:2).

Yield: 87%. M. pt.: 180–184 °C. Yellow color solid. Anal. Calc. for $C_{16}H_{11}NO_2S$ (%): C, 68.31; H, 3.94; N, 4.98; S, 11.40. Found: C, 68.45; H, 4.12; N, 4.82; S, 11.29. UV–Vis (DMSO): λ_{max}, nm (ε, dm^3 mol^{-1} cm^{-1}) 259 (22,900), 341 (11,000). FT-IR (KBr, cm^{-1}): 3327 (N–H), 1608 (C=O), 840 (C–S). ^{1}H NMR (500 MHz, $CDCl_3$): δ, ppm 9.29 (s, 1H, OCH), 8.39 (d, J = 8.0 Hz, 1H, NH), 8.03 (d, J = 8.1 Hz, 1H C*H*NH), 7.99 (d, J = 8.0 Hz, 1H, aromatic-H), 7.75 (t, J = 6.9, Hz, 1H, aromatic-H), 7.61–7.47 (m, 4H, aromatic-H), 7.43–7.36 (m, 2H, aromatic-H). ^{13}C NMR (125 MHz, $CDCl_3$): δ. ppm 174.8 (C=O), 158.6 (C–O), 156.5 (C–S), 155.9 (C–NH), 151.6, 136.1, 134.3, 126.3, 126.2, 126.2, 124.8, 123.8, 122.4, 121.6 (aromatic carbons).

2.2.2. Synthesis of 5-(1H-indol-3-yl)-4-methyl-2,4-dihydro-3H-1,2,4-triazole-3-thione (*SVS2*)

(*E*)-2-((1H-indol-3-yl)methylene)-N-methylhydrazine-1-carbothioamide (232 mg, 1 mmol) was added to methanol (7 mL) and refluxed for 10 min. To this, 1 mmol of anhydrous $FeCl_3$ (160 mg in 5 mL methanol) was added. The resulting solution was stirred at 60–65 °C for 6 h. Upon cooling the reaction solution in deep freezer, brown needle crystals suitable for XRD were formed.

Yield: 62%. M. pt.: 257–260 °C. Brown color solid. Anal. Calc. for $C_{11}H_{10}N_4S$ (%): C, 57.37; H, 4.38; N, 24.33; S, 13.92. Found: C, 57.22; H, 4.51; N, 24.18; S, 13.76. UV–Vis (DMSO): λ_{max}, nm (ε, dm^3 mol^{-1} cm^{-1}) 263 (24,300), 329 (12,050). FT-IR (KBr, cm^{-1}): 3423 (N–H), 3219 (N–H), 1540 (C=N), 1215 (C=S). ^{1}H NMR (500 MHz, DMSO–d_6): δ, ppm 13.77 (s, 1H, NH), 11.93 (s, 1H, indole NH), 8.08 (s, 1H, indole CH), 7.99 (d, J = 7.5 Hz, 1H, aromatic-H), 7.52 (d, J = 7.7 Hz, 1H, aromatic-H), 7.24 (t, J = 6.6 Hz, 1H, aromatic-H), 7.17 (t, J = 6.7 Hz, 1H, aromatic-H), 3.72 (s, 1H, CH_3). ^{13}C NMR (125 MHz, DMSO–d_6): δ. ppm 185.4 (C=S), 166.7 (C=N), 148.5,

136.4, 127.3, 125.5, 123.1, 121.0, 112.5, 101.4 (aromatic carbons), 32.1 (methyl carbon).

2.3. X-ray crystallography

Yellow block and brown block crystals of **SVS1** and **SVS2** of dimensions 0.56 × 0.54 × 0.44 mm and 0.54 × 0.21 × 0.16 mm, respectively, were chosen for the three-dimensional structural studies. Single crystal X-ray diffraction (XRD) data were collected at 110 K on an APEX K_α diffractometer using graphite monochromated MoK_α (λ = 0.70173 Å) radiation. The structure was solved using XT/XS in APEX2 [37,38] and refined by full matrix least squares on F^2 using Olex2 [39].

2.4. Quantum calculations, and molecular docking with SARS-CoV-2 M^{pro} and ACE-2, and molecular dynamics simulation

Materials Studio (DMol^3) software was used for optimization, and energy, HOMO (highest-occupied molecular orbital) and LUMO (lowest-unoccupied molecular orbital) calculations [40] of the compounds (**SVS1** and **SVS2**), and remdesivir, chloroquine and hydroxychloroquine drugs (Fig. 1). AutoDock-4.2 [41] was used for molecular docking of the compounds (**SVS1, SVS2**, remdesivir, chloroquine and hydroxychloroquine) at the active site of the enzymes, SARS-CoV-2 main protease and human ACE-2. For the preparation of ligands, the structures of the compounds were generated, Gasteiger charges were added, and polar hydrogen bonds were merged. These coordinates were saved in pdbqt format that contains the information about partial charges, atoms type and rotatable bonds. The 3D crystal structural coordinates of main protease of SARS-CoV-2 and human ACE-2 enzymes were retrieved from RCSB protein data bank with PDB IDs 6Y2F and 6M0J, respectively, and subjected to protein preparation (heteroatoms and water molecules were removed followed by assigning of polar hydrogen atoms and Kollman charges). The coordinates were saved in pdbqt format, and grid map for the active site was generated using Autogrid program. Docked complexes were analyzed using AutoDock tools. Active site interactions were generated using Ligplot plus [42].

Molecular dynamics simulation was performed for the best pose obtained from the docking of 6Y2F and **SVS1** using GROMACS version 2018.3 [43]. The protein complex was solvated using simple point-charge (SPC) water model in a cubic solvation box. The physiological pH in the protein structure was balanced by adding four sodium ions to the solvent molecules, bringing the entire system to a neutral charge. By using the steepest descent algorithm, the energy minimization was carried out for a maximum of 50,000 steps. After the model structures were converged to a maximum force, a two-step equilibration *via* the NVT (where N is amount of substance, V is volume and T is temperature) canonical ensemble (isothermal-isochoric) equilibration was performed for 100 picoseconds (ps) at 300 K with Berendsen thermostat temperature coupling. This was followed by a constant number of particles, pressure and temperature (NPT) ensemble equilibration for another 100 ps. The LINCS (linear constraint solver) algorithm was used to constraint the covalent bonds. To treat the long-range coulombic interactions, the particle mesh Ewald (PME) method [44] was used. Production MD was carried out at a constant temperature of 300 K using the NPT ensemble for 50 ns and the MD trajectories were saved for every 10 ps. MD analysis of trajectories was done using Gromacs in-built utilities like gmx RMS, RMSF, gyrate and cluster. The conformations were visualized and images were generated using Pymol [45].

2.5. In vitro cytotoxicity

HepG-2 (hepatic carcinoma), T24 (bladder), EA.hy926 (endothelial) and Vero (kidney epithelial normal cells extracted from an African green monkey) cells were used for testing cytotoxicity of the compounds (**SVS1** and **SVS2**) and most commonly used anticancer agents (cisplatin and doxorubicin) using MTT [3-(4,5-dimethylthiazol-2yl)-2,5-diphenyltetraazolium bromide] assay. HepG-2 and EA.hy926 cancer cells were maintained in DMEM (Dulbecco's modified Eagle's medium), T24 cancer cells in McCoy's 5a medium and Vero normal cells in RPMI-1640 (Roswell Park Memorial Institute) medium. Cells were plated in 96-well plates at a concentration of 1 × 10^4 cells per well in suitable medium and incubated for 24 h at 37 °C. Then compounds to be tested with the known concentration (0–50 or 100 µM) were seeded into the wells after dissolving them in DMSO. At the end of the incubation (24 h) of plates, the MTT dye solution (10 µL, 5 mg/mL) was added per well in dark at 37 °C for 4 h, and 100 µL of DMSO was added, and the absorbance of compounds was measured at 570 nm. IC_{50} values were determined as the concentration of corresponding compound that produced a 50% reduction of cell viability [46].

3. Results and discussion

3.1. Synthesis of azole-based heterocyclic compounds

As seen in Scheme 1, 3-(2,3-dihydrobenzo[d]thiazol-2-yl)-4H-chromen-4-one (**SVS1**) was synthesized by reacting 2-aminothiophenol with 4-oxo-4H-chromene-3-carbaldehyde in C_2H_5OH under reflux condition for 4 h. 5-(1H-indol-3-yl)-4-methyl-2,4-dihydro-3H-1,2,4-triazole-3-thione (**SVS2**) was prepared from (*E*)-2-((1H-indol-3-yl)methylene)-N-methylhydrazine-1-carbothioamide [34–36,47] in methanol at 60–65 °C in the presence of anhydrous $FeCl_3$ at reflux condition for 6 h, as indicated in Scheme 2. These types of cyclization reactions are rarely reported in the literature, and it might be a key reaction for developing new bioactive heterocyclic drugs in the future. Both the compounds were adequately characterized using UV-Visible, FT-IR and NMR spectroscopic techniques. The three-dimensional structures of **SVS1** and **SVS2** were confirmed by single crystal XRD and validated by DFT calculations. **SVS1** was soluble in most of organic solvents such as CH_2Cl_2, $CHCl_3$, DMF, DMSO, *etc*., whereas **SVS2** was soluble in DMF and DMSO solvents.

3.2. FT-IR and UV-Visible spectroscopy

In the FT-IR spectrum of **SVS1**, two bands observed at 3327 and 1608 cm^{-1} were assigned to υN–H and υC=O, respectively (Fig. S1). In addition, a band appeared at 840 cm^{-1} due to C–S stretching. The spectrum of **SVS2** showed indole and triazole N–H stretching frequencies at 3423 and 3219 cm^{-1}, respectively. Also, two bands at 1215 and 1540 cm^{-1} characteristic of υ(C=S) and υ(C=N) stretching frequencies, respectively, were detected [24]. The compounds showed two bands in their UV-Visible spectra corresponding to $\pi \rightarrow \pi^*$ and $n \rightarrow \pi^*$ electronic transitions in the ranges of 259–263 and 329–341 nm, respectively [22,23].

3.3. ^1H and ^{13}C NMR spectroscopy

The NMR (^{1}H and ^{13}C) spectra of **SVS1** and **SVS2** were recorded in $CDCl_3$/DMSO–d_6 solvent, and spectra are shown in Figs. S2 and S3. In the ^{1}H NMR spectrum of **SVS1**, the signals of OCH, C*H*NH and NH were observed at 9.29, 8.03 and 8.0 ppm, respectively. In addition, a doublet and triplet signals were seen in the region 7.99–7.47 ppm, corresponding to the aromatic protons. In the ^{1}H NMR spectrum of **SVS2**, the signals due to the NH protons (from

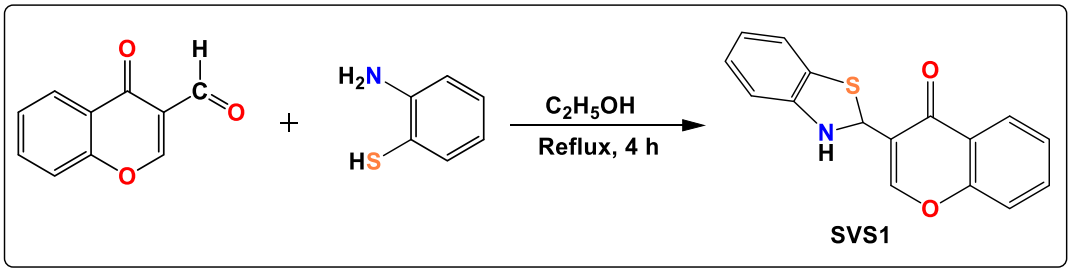

Scheme 1. Synthetic route for chromone-based thiazole compound (**SVS1**).

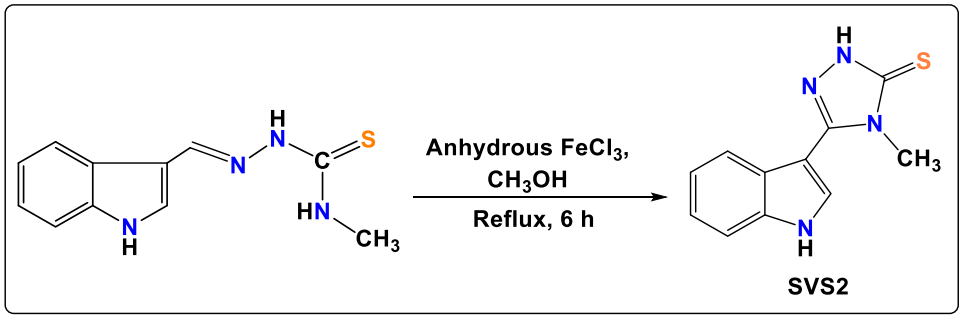

Scheme 2. Synthetic route for indole-based triazole compound (**SVS2**).

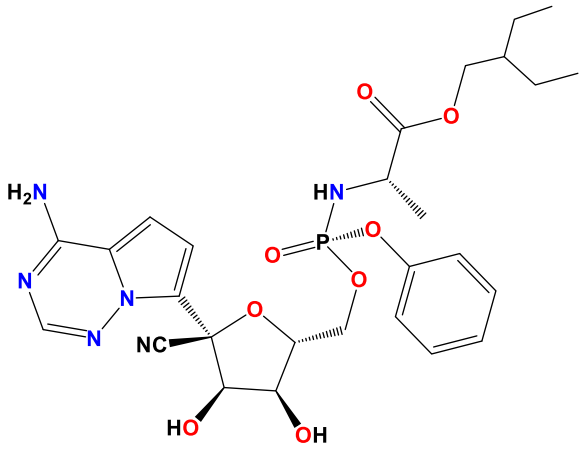

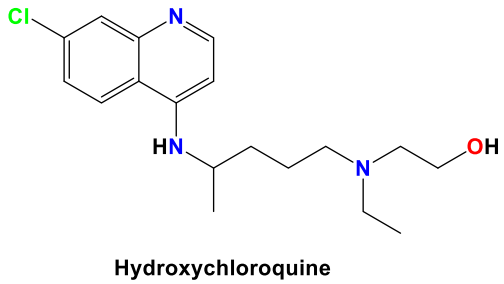

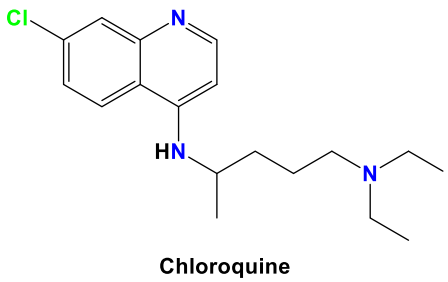

Fig. 1. Structure of remdesivir, hydroxychloroquine and chloroquine.

triazole and indole) and indole CH proton appeared at 13.77 (triazole) / 11.93 (indole) and 8.08 ppm, respectively. The signals of phenyl ring protons of **SVS2** were displayed at 7.99–7.17 ppm. A signal at 3.72 ppm is related to the protons of methyl group [48].

The ^{13}C NMR spectra of **SVS1** and **SVS2** are shown in Figs. S4 and S5, respectively. The C=O carbon resonated at 174.8 ppm in the spectrum of **SVS1**. Moreover, the C–S, C–O and C–NH carbons resonated at 156.5, 158.6 and 155.9 ppm, respectively. In the ^{13}C NMR spectrum of **SVS2**, a signal was observed at 185.4 ppm for carbon of C=S, while a peak related to carbon of C=N was observed at 166.7 ppm. In addition, signal of methyl carbon was observed at 32.1 ppm. The aromatic carbon signals

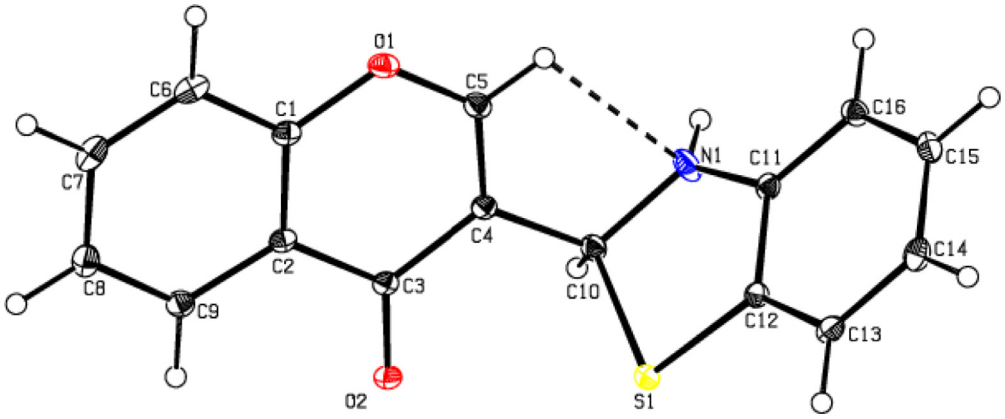

Fig. 2. Molecular structure of **SVS1** drawn at 30% probability level. Intra-molecular interaction is represented as dashed line.

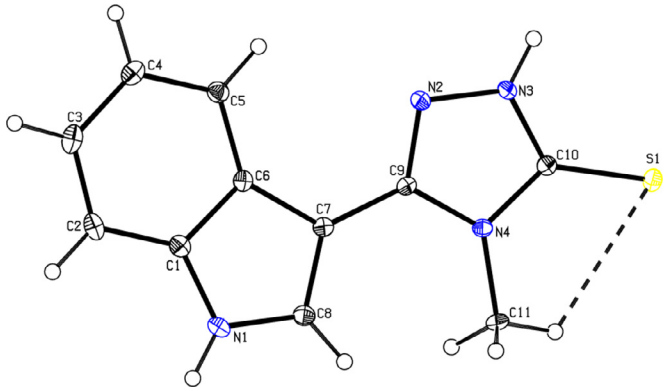

Fig. 3. Molecular structure of **SVS2** drawn at 30% probability level. Intra-molecular interaction is represented as dashed line.

of both the compounds were observed in their corresponding region.

3.4. Description of crystal structures

Three-dimensional crystal structures of **SVS1** and **SVS2** were refined to good R factor of 3.6 and 2.4%, respectively. Thermal ellipsoidal plots of **SVS1** and **SVS2** are given in Figs. 2 and 3, respectively. All the bond lengths and angles were in the allowed ranges (Tables 1–3). In **SVS1**, O2 is planar with the ring (C1−C2−C3−C4−C5−O1) as evident from the torsion angle O2−C3−C2−C1 [−179.8(1)°]. The five membered ring (C10−N1−C11−C12−S1) adopted twisted conformation with twist on S1−C10, and the puckering parameters are Q(2) = 0.208(1) Å and $\varphi(2)$ = 205.0(4)°. The molecular structure was stabilized by C−H···N intramolecular interaction which generates S(5) pattern (Fig. 4, Table 4). Crystal packing was stabilized by N−H1···O2 (x, -*y* + 3/2, *z* + 1/2) intermolecular hydrogen bond, generating chain C(6) (Fig. 4). As compound **SVS2** crystallized in non-centrosymmetric space group $P2_12_12_1$, the absolute structure was relevant and the Flack parameter, x [0.046(16)], was determined using 929 quotients [(*I*+) − (I−)] / [(I+) + (I−)]. The crystal structure of **SVS2** was nearly planar. Torsion angles C11−N4−C10−N3 [176.6(2)°] and S1−C10−N3−N2 [−179.1(1)°] indicated that C11 and S1 were almost in-plane with a five membered ring to which they were attached. The molecular structure of **SVS2** was stabilized by C−H···S intramolecular interaction, generating S(5) pattern (Fig. 4b). The crystal packing was stabilized by N−H···S and N−H···N intermolecular hydrogen bonds. Atoms N1 and N3 in the molecule at x, y, z act as donors to atoms S1 and N2 at -*x* + 1, y-1/2, -*z* + 1/2 and x-1/2, -*y* + 3/2, -*z* + 1, generating C(8) and C(3) chains, respectively (Fig. 4b).

3.5. Quantum chemical calculations

We optimized the compounds to obtain energies, HOMO and LUMO in Materials Studio software. **SVS1, SVS2** and the drugs (chloroquine, hydroxychloroquine and remdesivir) were optimized and are shown in Fig. 5. DMol^3 module, based on the first principles of electronic structure calculations, in the Materials Studio was used to calculate the electronic properties; basis set properties, core treatment, effective core potential and molecular orbitals – HOMO and LUMO. The electron charge distributions of the HOMO and LUMO are shown in Fig. 6. The HOMO and LUMO energies of **SVS1** were found to be −0.2112 and −0.1080 eV, respectively. The band gap energy ($\Delta E = E_{LUMO} - E_{HOMO}$) of **SVS1** was calculated to be 0.1032 eV. The HOMOs were principally localized on N of thiazole and benzene ring linked to thiazole ring as well as oxygen atoms of chromone. The LUMOs were largely localized on O, C and H atoms of benzopyran-4-one and benzene linked to benzopyran-4-one as well as, S and N of thiazole ring and carbons of benzene linked to thiazole. The total energy, kinetic energy, electrostatic energy and binding energy for **SVS1** were estimated to be −1211.6113, −12.9679, 2.5631, and −6.4527 kcal/mol, respectively. Meanwhile, the HOMO and LUMO energies of **SVS2** were found to be −0.1916 and −0.0735 eV, respectively. The calculated energy gap between HOMO and LUMO of **SVS2** was found to be 0.1181 eV (Table 5). The HOMOs were largely localized on the N and S atoms of triazole as well as N and ethylene (C=C) of pyrrole, while the LUMOs were localized on the N atoms of triazole and benzene ring, as well as N and C–C of pyrrole. The total energy, kinetic energy, electrostatic energy and binding energy of **SVS2** were evaluated to be −1036.7616, −10.7901, 1.9682, and −5.2075 kcal/mol, respectively. The HOMO energies of remdesivir, hydroxychloroquine and chloroquine were estimated to be −0.1865, −0.1973 and −0.2047 eV, respectively. Meanwhile, the LUMO energies of remdesivir, hydroxychloroquine and chloroquine were found to be −0.1055, −0.0798 and −0.0884 eV, respectively. The band gap energies of remdesivir, hydroxychloroquine and chloroquine were seen as 0.0810, 0.1175 and 0.1163 eV, respectively. The HOMO of remdesivir was largely localized on the cyanide, N and C atoms of pyrrole, while the LUMOs were localized on cyanide, N and C atoms of pyrrole and triazine as well as primary amine linked to triazine. The total energy, kinetic energy, electrostatic energy and binding energy of remdesivir were found to be −2321.2748, −31.2326, 6.7183, and −14.5585 kcal/mol, respectively. HOMO of hydroxychloroquine can be related to the aromatic rings and secondary amine while the LUMO can be assigned

Table 1
X-ray diffraction data collection, structure determination and refinement details for **SVS1** and **SVS2**.

	SVS1	**SVS2**
CCDC number	2053105	2053106
Chemical formula	$C_{16}H_{11}NO_2S$	$C_{11}H_{10}N_4S$
Radiation type, Wavelength	MoKα, 0.71073	
M_r	281.32	230.29
Crystal system, Space group	Monoclinic, $P2_1/c$	Orthorhombic, $P2_12_12_1$
Temperature (K)	110	
Unit cell dimensions (Å, °)	a = 7.2434(15), b = 14.400(3), c = 12.084(3), β = 92.683(3)	a = 4.9842(7), b = 12.2295(17), c = 17.006(2)
V (Å^3)	1259.0(5)	1036.6(3)
Z, D_x (Mg m^{-3})	4, 1.484	4, 1.476
Absorption coefficient (μ) (mm^{-1})	0.26	0.287
F(000)	584	480
Color, Crystal size (mm)	Yellow, 0.56 × 0.54 × 0.44	Brown, 0.54 × 0.21 × 0.16
θ_{min}, θ_{max} (°)	2.2, 27.4	2.1, 27.4
No. of measured, independent and observed [I > 2σ(I)] reflections	22,959, 2875, 2580	22,333, 2357, 2303
Index ranges	h = −9→9 k = −18→18 l = −15→15	h = −6→6 k = −15→15 l = −22→21
Absorption correction	Multi-scan	
T_{min}, T_{max}	0.649, 0.746	0.690, 0.746
Refinement method	Full matrix least-squares on F^2	
No. of reflections, restraints, parameters	2875, 0, 182	2357, 0, 146
R_{int}	0.040	0.024
sin θ/λ_{max} (Å^{-1})	0.648	0.647
H-atom treatment	Mixed	Constrained
R [$F^2>2\sigma(F^2)$], wR(F^2)]	0.036, 0.093	0.024, 0.063
Final R indices [I>2sigma(I)]	R1 = 0.036, wR2 = 0.090	R1 = 0.024, wR2 = 0.063
R indices (all data)	R1 = 0.041, wR2 = 0.093	R1 = 0.025, wR2 = 0.063
Goodness of fit on F^2 (S)	1.08	1.06
Absolute structure parameter	–	0.046(16)
$\Delta\rho_{max}$, $\Delta\rho_{min}$ (e Å^{-3})	0.28, −0.34	0.23, −0.14

Table 2
Selected geometric parameters (Å, °).

Bond length (Å)/angle (°)	**SVS1**	Bond length (Å)/angle (°)	**SVS2**
S(1)–C(10)	1.8599(15)	S(1)–C(10)	1.6903(18)
S(1)–C(12)	1.7624(15)	N(1)–C(8)	1.358(2)
O(1)–C(1)	1.3746(18)	N(2)–N(3)	1.375(2)
O(1)–C(5)	1.356(2)	N(3)-C(10)	1.332(2)
O(2)–C(3)	1.2368(18)	N(4)–C(10)	1.371(2)
N(1)–C(10)	1.4495(19)	N(4)–C(9)	1.384(2)
N(1)–C(11)	1.393(2)	N(2)–C(9)	1.319(2)
C(12)–S(1)–C(10)	90.60(7)	N(4)–C(11)	1.458(2)
C(5)–O(1)–C(1)	118.32(12)	C(8)–N(1)–C(1)	109.18(15)
O(1)–C(1)–C(2)	121.90(14)	C(9)–N(2)–N(3)	104.41(13)
O(1)–C(1)–C(6)	116.24(13)	N(3)–C(10)–N(4)	104.31(15)
N(1)–C(10)–S(1)	105.44(10)	C(10)–N(3)–N(2)	113.21(14)
N(1)–C(10)–C(4)	113.86(13)	N(4)–C(10)–S(1)	128.25(13)
C(4)–C(10)–S(1)	108.38(10)	C(9)–N(4)–C(11)	128.03(15)
N(1)–C(11)–C(12)	113.94(13)	C(10)–N(4)–C(9)	108.06(13)
C(16)–C(11)–N(1)	126.48(14)	N(1)–C(1)–C(2)	128.95(17)
C(11)–C(12)–S(1)	111.74(11)	N(1)–C(1)–C(6)	107.94(16)
C(11)–N(1)–C(10)	114.51(12)	N(1)–C(8)–C(7)	110.26(16)
C(13)–C(12)–S(1)	127.03(12)	N(2)–C(9)–N(4)	110.00(14)
		N(3)–C(10)–S(1)	127.45(13)

to the N linked to 7-chloroquinoline and N of quinoline. The total energy, kinetic energy, electrostatic energy and binding energy of chloroquine were found to be −1316.7732, −16.4052, 1.9865, and −8.6195 kcal/mol, respectively. HOMOs and LUMOs of chloroquine were localized on 7-chloroquinoline moiety and N linked to 7-chloroquinoline.

3.6. Quantum chemical parameters

The module DMol^3 in Materials Studio 2017 was used to calculate quantum chemical parameters such as chemical potential (μ), global hardness (η), global softness (σ), absolute electronegativity (χ) and electrophilicity index (ω) for the studied compounds [49].

3.6.1. Global hardness (η) and electronegativity (χ)

To describe the chemical and biological reactivity ranking of **SVS1** and **SVS2**, various electronic parameters such as ionization potential (I), electron affinity (A), absolute electronegativity (χ) and chemical hardness (η) were calculated. I and A were calculated as the negative of energy values of HOMO and LUMO, respectively (Table 5).

Table 3
Selected torsion angles (°).

Torsion angle (°)	**SVS1**	Torsion angle (°)	**SVS2**
S(1)–C(12)–C(13)–C(14)	176.01(12)	N(1)–C(1)–C(2)–C(3)	179.81(18)
O(1)–C(1)–C(2)–C(3)	0.2(2)	N(1) –C(1)–C(6)–C(5)	178.60(16)
O(1)–C(1)–C(2)–C(9)	−179.70(12)	N(1)–C(1)–C(6)–C(7)	−1.04(19)
O(1)–C(1)–C(6)–C(7)	179.97(13)	N(2)–N(3)–C(10)–S(1)	−179.07(12)
O(2)–C(3)–C(4)–C(5)	179.21(13)	N(2)–N(3)–C(10)–N(4)	1.16(19)
O(2)–C(3)–C(4)–C(10)	−1.3(2)	N(3)–N(2)–C(9)–N(4)	0.04(18)
N(1)–C(11)–C(12)–S(1)	3.35(17)	N(3)–N(2)–C(9)–C(7)	179.88(14)
N(1)–C(11)–C(12)–C(13)	−179.73(14)	C(1)–N(1)–C(8)–C(7)	−0.3(2)
N(1)–C(11)–C(16)–C(15)	−179.76(15)	C(6)–C(7)–C(8)–N(1)	−0.39(19)
C(1)–C(2)–C(3)–O(2)	−179.75(13)	C(6)–C(7)–C(9)–N(2)	5.2(3)
C(3)–C(4)–C(5)–O(1)	0.9(2)	C(6)–C(7)–C(9)–N(4)	−174.97(16)
C(3)–C(4)–C(10)–S(1)	−64.88(14)	C(8)–N(1)–C(1)–C(2)	−179.26(18)
C(3)-C(4)-C(10)-N(1)	178.14(12)	C(8)–N(1)–C(1)–C(6)	0.8(2)
C(5)–C(4)–C(10)–S(1)	114.55(14)	C(8)–C(7)–C(9)–N(2)	−171.56(17)
C(5)–C(4)–C(10)–N(1)	−2.4(2)	C(8)–C(7)–C(9)–N(4)	8.3(3)
C(9)–C(2)–C(3)–O(2)	0.2(2)	C(9)–N(2)–N(3)–C(10)	−0.77(19)
C(9)–C(2)–C(3)–C(4)	−179.43(13)	C(9)–N(4)–C(10)–S(1)	179.16(13)
C(10)–S(1)–C(12)–C(11)	−12.31(12)	C(9)–N(4)–C(10)–N(3)	−1.07(18)
C(10)–S(1)–C(12)–C(13)	170.99(14)	C(9)–C(7)–C(8)–N(1)	176.88(16)
C(10)–N(1)–C(11)–C(12)	11.4(2)	C(10)–N(4)–C(9)–N(2)	0.66(19)
C(10)–N(1)–C(11)–C(16)	−168.96(15)	C(10)–N(4)–C(9)–C(7)	−179.17(15)
C(10)–C(4)–C(5)–O(1)	−178.50(13)	C(11)–N(4)–C(9)–N(2)	175.91(15)
C(11)–N(1)–C(10)–S(1)	−19.35(16)	C(11)–N(4)–C(9)–C(7)	−3.9(3)
C(11)–N(1)–C(10)–C(4)	99.32(16)	C(11)–N(4)–C(10)–S(1)	3.7(2)
C(12)–S(1)–C(10)–N(1)	17.36(11)	C(11)–N(4)–C(10)–N(3)	−176.58(15)
C(12)–S(1)–C(10)–C(4)	−104.91(11)	C(1)–C(2)–C(3)–C(4)	1.5(3)
C(16)–C(11)–C(12)–S(1)	−176.36(11)	C(1)–C(6)–C(7)–C(8)	0.88(18)

Table 4
Intra- and inter-molecular hydrogen bonding interactions.

Donor–Hydrogen···Acceptor	D–H (Å)	H···A (Å)	D···A (Å)	D–H···A (°)
SVS1				
C5–H5···N1	0.95	2.42	2.818(2)	105
N1–H1···O2 (x, -y+3/2, z+1/2)	0.87	2.16	2.980(2)	156
SVS2				
C11–H11B···S1	0.98	2.74	3.230(2)	111
N1–H1···S1 (-x+1, y-1/2, -z+1/2)	0.88	2.44	3.309(2)	169
N3–H3···N2 (x-1/2, -y+3/2, -z+1)	0.88	2.03	2.893(2)	167

Table 5
Important thermodynamic parameters obtained by Materials Studio simulation.

	SVS1	**SVS2**
Global and chemical reactivity descriptor	(eV)	(eV)
Energy of HOMO	–0.211	–0.1916
Energy of LUMO	–0.108	–0.0735
Energy gap [ΔE = LUMO – HOMO]	0.103	0.1181
Ionization energy [$I = -E_{HOMO}$]	0.211	0.1916
Electron affinity [$A = -E_{LUMO}$]	0.108	0.0735
Chemical hardness (η) [(I–A)/2]	0.051	0.0590
Chemical potential (μ) [1/2 ($E_{HOMO} + E_{LUMO}$)]	–0.159	–0.1325
Softness (σ) [$1/\eta$]	19.379	16.9491
Electrophilicity index (ω) [$\mu^2/2\eta$]	5.172	5.0102

The chemical reactivity of molecules increased with the increasing of I. Systems having high E_{HOMO} such as DNA are good electron donors, and drugs or synthesized compounds having low E_{LUMO} are good electron acceptors [50]. So, with more negative E_{LUMO}, chemical reactivity of molecules increased as electron acceptor. The electron affinity value (A) of **SVS2** (0.0735 eV) was lower than that of **SVS1** (0.1080 eV). So, **SVS2** may be able to interact with the targeted biomolecules (DNA or protein) better than **SVS1** due to more negative E_{LUMO} [6]. The band gap is an important parameter to determine some of the molecular properties such as global hardness (η), electronegativity (χ), chemical potential (μ) and global electrophilicity index (ω) (Table 4). If energy gap is decreased, it leads to less stability, high kinetic energy, high chemical reactivity and more polarization [51]. The hardness (η) of the compounds was calculated using Eq. (1) and values are given in Table 5 [40].

$$\eta = \left(\frac{I - A}{2}\right) \tag{1}$$

I and A are the ionization potential and electron affinity of the molecules, respectively. The calculated energy gap values of **SVS1** and **SVS2** were 0.1032 and 0.1181 eV, respectively. The energy gap of **SVS2** was more than that of **SVS1**, indicating that the chemical reactivity of **SVS2** was less compared to **SVS1**. To explain the chemical reactivity, the hardness and softness of compounds are important parameters. With the increasing of softness, chemical reactivity is increased. Meanwhile, increase of hardness leads to decrease of chemical reactivity. The hardness of **SVS1** (0.0516 eV) was lower than that of **SVS2** (0.0590 eV). As a result, the chemical reactivity of **SVS1** was more. In addition, **SVS2** had high stability and polarization [52].

3.6.2. Chemical potential (μ) and electrophilicity power (ω)

Chemical potential (μ) can be associated with the electron withdrawing capability [51]. The values of chemical potential (μ) of **SVS1** and **SVS2** were −1.5664 and −1.8860 eV, respectively. As a result, **SVS2** had more chemical potential (μ) and electronegativity (χ) than **SVS1** [3,51]. In addition, chemical potential (μ) is associated to the adsorptive capacity. An elevated value of chemical potential showed enhanced adsorption between molecules and biological systems as well as the adsorbent surfaces. Therefore, the

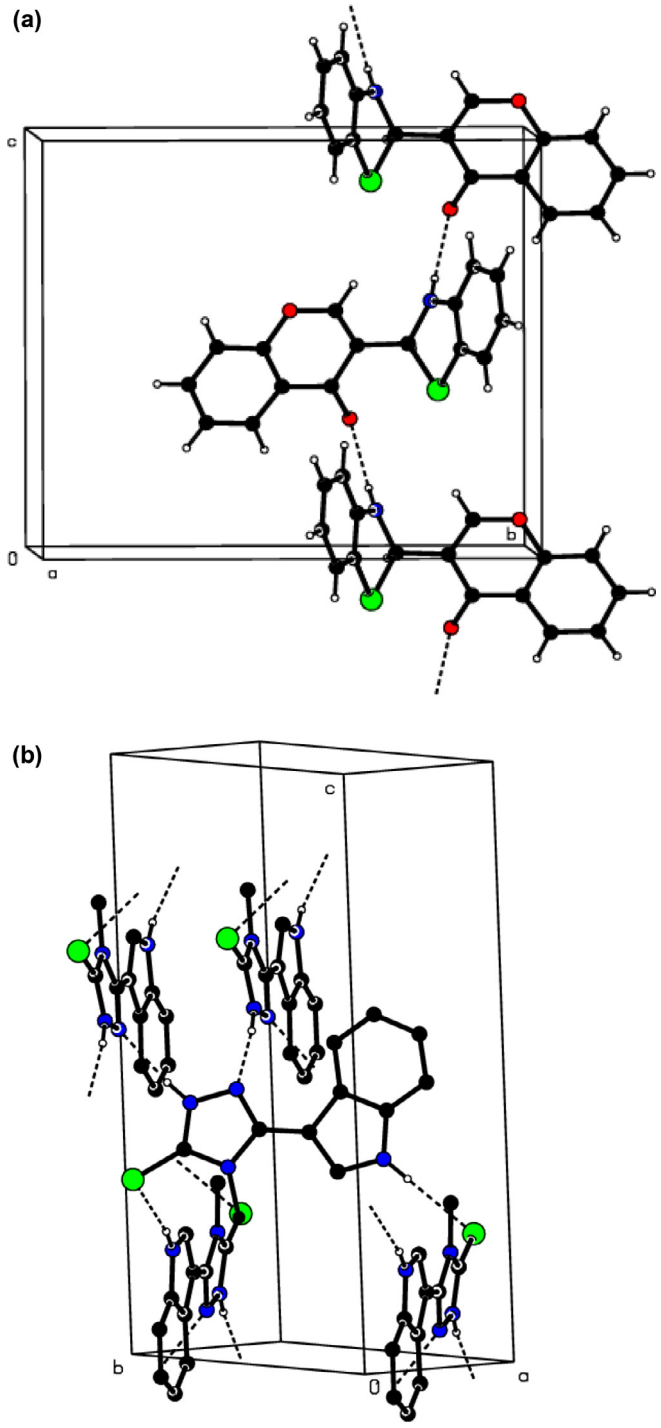

Fig. 4. Packing diagram showing inter-molecular hydrogen bonding interactions in (a) **SVS1** and (b) **SVS2**.

high value of chemical potential can cause electron transfer from a molecule to biological systems. As a result, electrons of **SVS2** can be transferred easily to the biological systems.

The electrophilicity index (ω) can be calculated using the chemical potential and chemical hardness (Eq. (2)) [52,53].

$$\omega = \frac{(\eta)^2}{2\eta} \tag{2}$$

The electron accepting ability of a molecule from the surrounding without changing its stability is referred to electrophilicity index (ω) [51]. In addition, the toxicity of compounds such as antimicrobial, anticancer, *etc*., can be estimated through electrophilicity index (ω) [54]. A compound with a low electrophilicity index is anticipated to have less toxicity [55]. The electrophilicity index (ω) values for **SVS1** and **SVS2** were 23.7752 and 30.1440 eV, respectively (Table 5). The higher value of electrophilicity index (ω) for **SVS2** can be correlated with its less toxicity. So, low concentration of **SVS2** is enough to kill cancer cells [29,30].

3.7. Molecular docking with SARS-CoV-2 M^{pro} and ACE-2, and molecular dynamics simulation

Coronaviruses have enveloped structures, their RNA is positive, and have very long single stranded RNA. SARS-CoV-2 has structural and non-structural proteins. One of the most important structural proteins is spike glycoprotein (S). For the entry of SARS-CoV into the host cell, spike glycoprotein (S) binds with the host receptor and angiotensin-converting enzyme-2 (ACE-2) [31,32]. In addition, papain-like protease (PL^{pro}) and 3-chymotrypsin-like protease ($3CL^{pro}$ or M^{pro}) are non-structural proteins that are essential for the replication of the virus. SARS-CoV-2 main protease is made up of three domains. The active site of protein lies at the interface of domain I and domain II and contains a characteristic Cys-His dyad. A linker joins domain II to domain III, which is critical for the dimerization of protein.

It must be emphasized that the action of a viral spike protein is one of the most important pathophysiological mechanisms that facilitates the virus to enter into the host with the aid of ACE-2 receptor. Hepacidin, regulator of iron metabolism, interacts with ferroportin to facilitate the entry of iron into the cells. In SARS-CoV-2 infection, iron metabolism dysfunction occurs in extreme cases leading to ferroptosis. Iron metabolism dysfunction plays a major role in multi-organ failure [56]. As a result, anemic hypoxia creates lung disease. The above mentioned facts have shown ways to create effective protocols for the treatment of COVID-19 disease including (a) a drug that obstructs the life cycle of the virus by blocking ACE-2 receptors or inhibiting SARS-CoV-2 main protease (M^{pro}) [57], (b) an iron chelating agent to conjugate with the excess iron resulting from its dysmetabolism, and (c) anti-inflammatory drugs as phosphodiesterase-4 inhibitors for the treatment of lung inflammation and necrosis [32,34].

In our study, the synthesized heterocyclic compounds (**SVS1** and **SVS2**) were screened against the SARS-CoV-2 main protease (M^{pro}) enzyme and human ACE-2 receptor through molecular docking. The structures of our compounds are similar to some commercially available drugs containing thiazole, 1,3,4-oxadiazole and heterocyclic moieties (Fig. 7). Amongst the coronavirus targets, the main protease (M^{pro}) has received a major attention [58,59], and ACE-2 plays a critical role for SARS-CoV to enter into target cells. So, ACE-2 is also one of the key targets for therapeutic development [36,37] of antiviral drugs against SARS-CoV-2. The crystal structure of SARS-CoV-2 spike receptor-binding domain bound with ACE-2 (PDB ID: 6M0J) contains two chains, where chain A represents the angiotensin-converting enzyme-2 and chain E is the spike receptor binding domain. Only chain A of 6M0J (ACE-2) was used for the present docking study. The docking results showed that both the compounds can effectively bind with the molecular targets SARS-CoV-2 main protease and human ACE-2. The docking energies of **SVS1, SVS2**, remdesivir, chloroquine and hydroxychloroquine with SARS-CoV-2 M^{pro} and human ACE-2 are shown in Table 6. Figs. 8 and 9 show the interactions of the compounds at the active site of the enzymes, SARS-CoV-2 main protease and human ACE-2, respectively. The docking results showed that both **SVS1** and **SVS2** had maintained comparable interactions at the active site of the enzymes when compared to remdesivir (SARS-CoV-2), chloroquine and hydroxychloroquine.

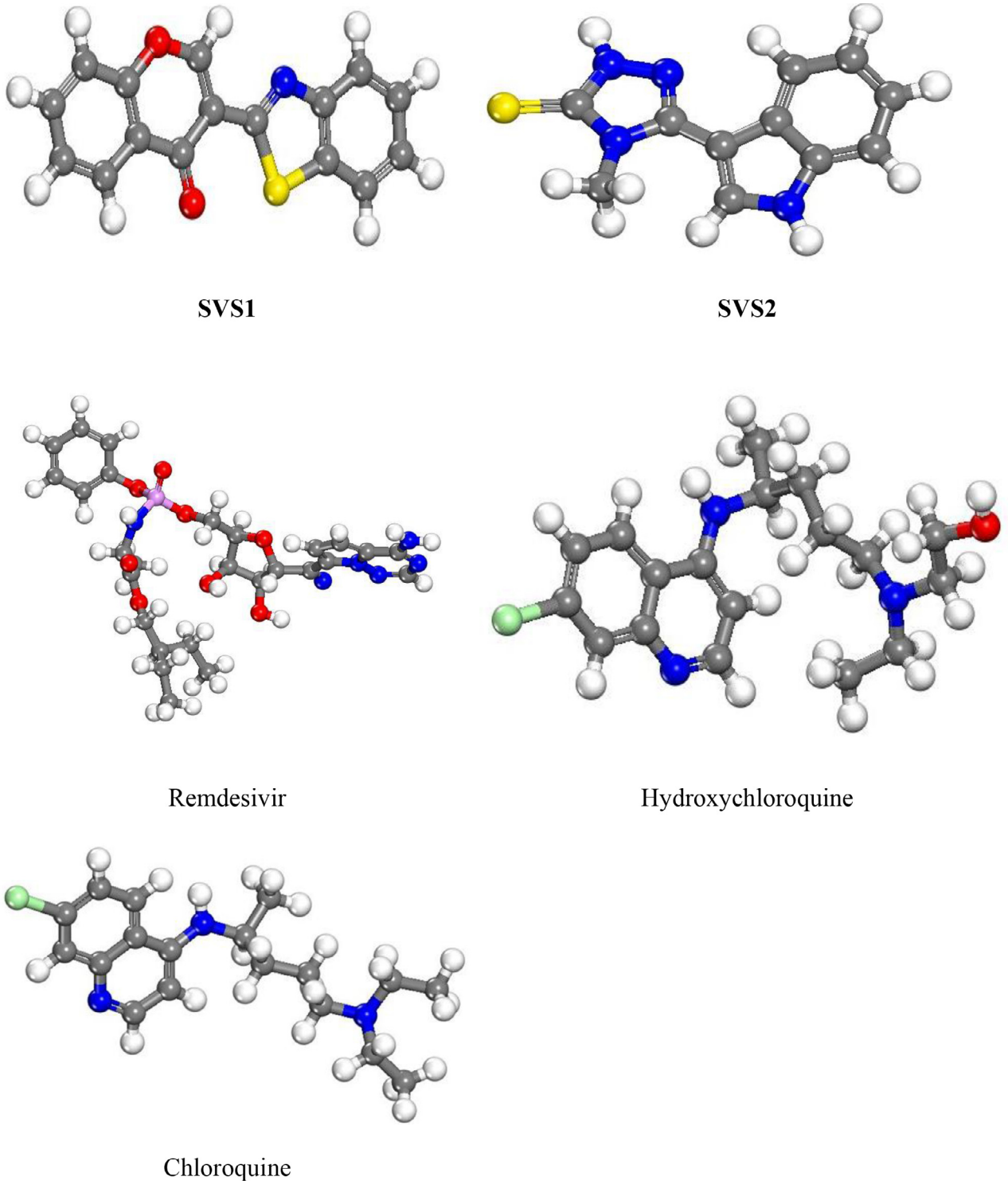

Fig. 5. Optimized structures of **SVS1**, **SVS2**, remdesivir, hydroxychloroquine and chloroquine (DMol^3 module in Materials Studio 2017 was used).

50 ns molecular dynamics simulation (MDS) of the SARS-CoV-2 main protease and **SVS1** complex was performed to study the stability and conformational changes. The stability of the complex was initially assessed by plotting the root mean square deviation (RMSD). From the RMSD graph (Fig. 10), it was observed that the RMSD values were approximately between 0.25 and 0.37 nm. The deviation in the RMSD was calculated to be ~0.12 nm. Less RMSD deviation confers that **SVS1** remained within the active site pocket of the enzyme throughout the simulation but maintained the dynamic nature within the active site. RMSF (root-mean-square fluctuation) analysis was done to study the average per-residue fluctuations during MDS. From the RMSF graph (Fig. 10), it was observed that the RMSF varied between 0.1 and 0.35 nm with the highest fluctuation of 0.5 nm for the N-terminal atoms. High fluctuation in RMSF is usually observed for the terminal atoms. The radius of gyration was plotted based on the Cα atoms of the protein, it was noted that the values ranged between 2.15 and 2.25 nm.

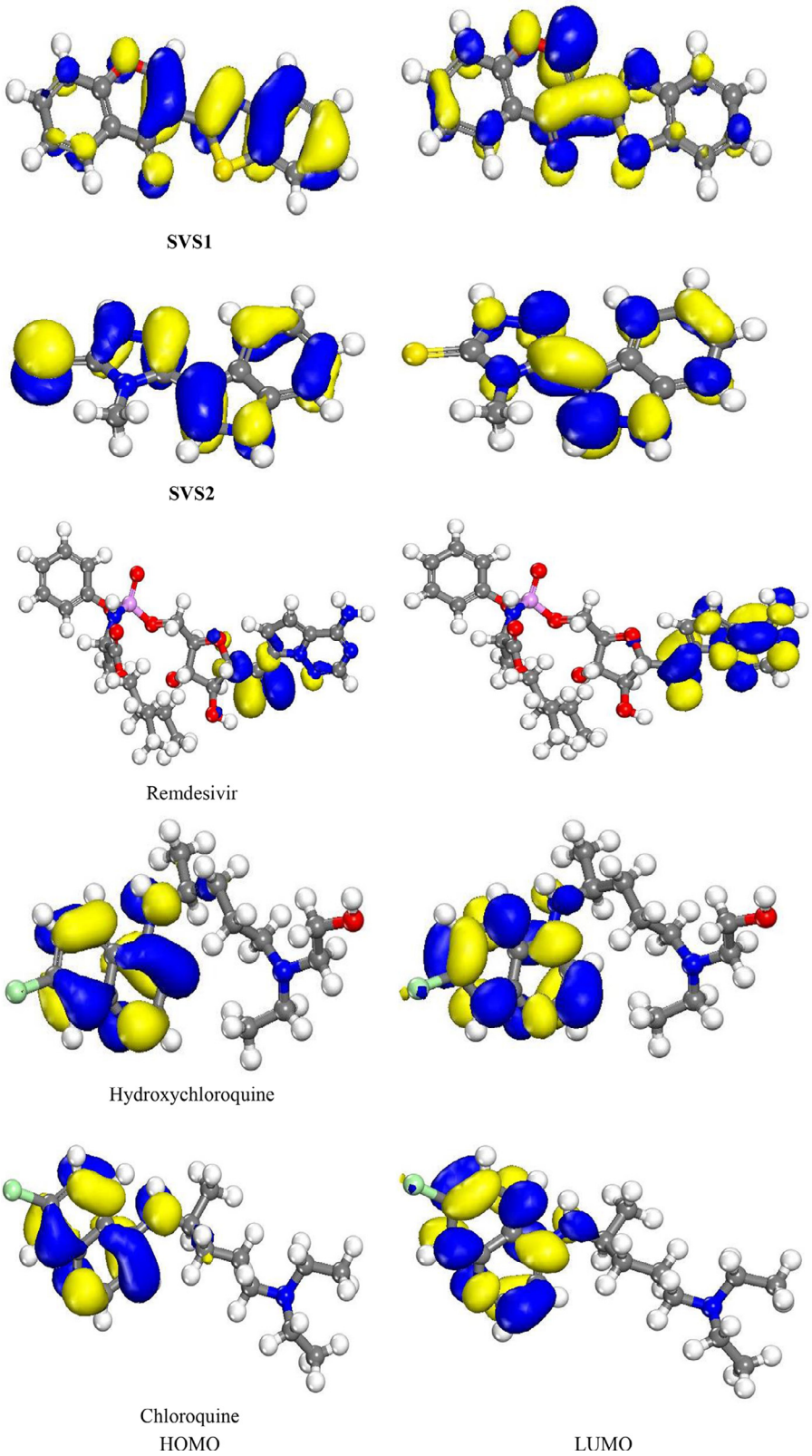

Fig. 6. Perspective views of the obtained HOMO and LUMO of **SVS1**, **SVS2**, remdesivir, hydroxychloroquine and chloroquine (DMol^3 module in Materials Studio 2017 was used).

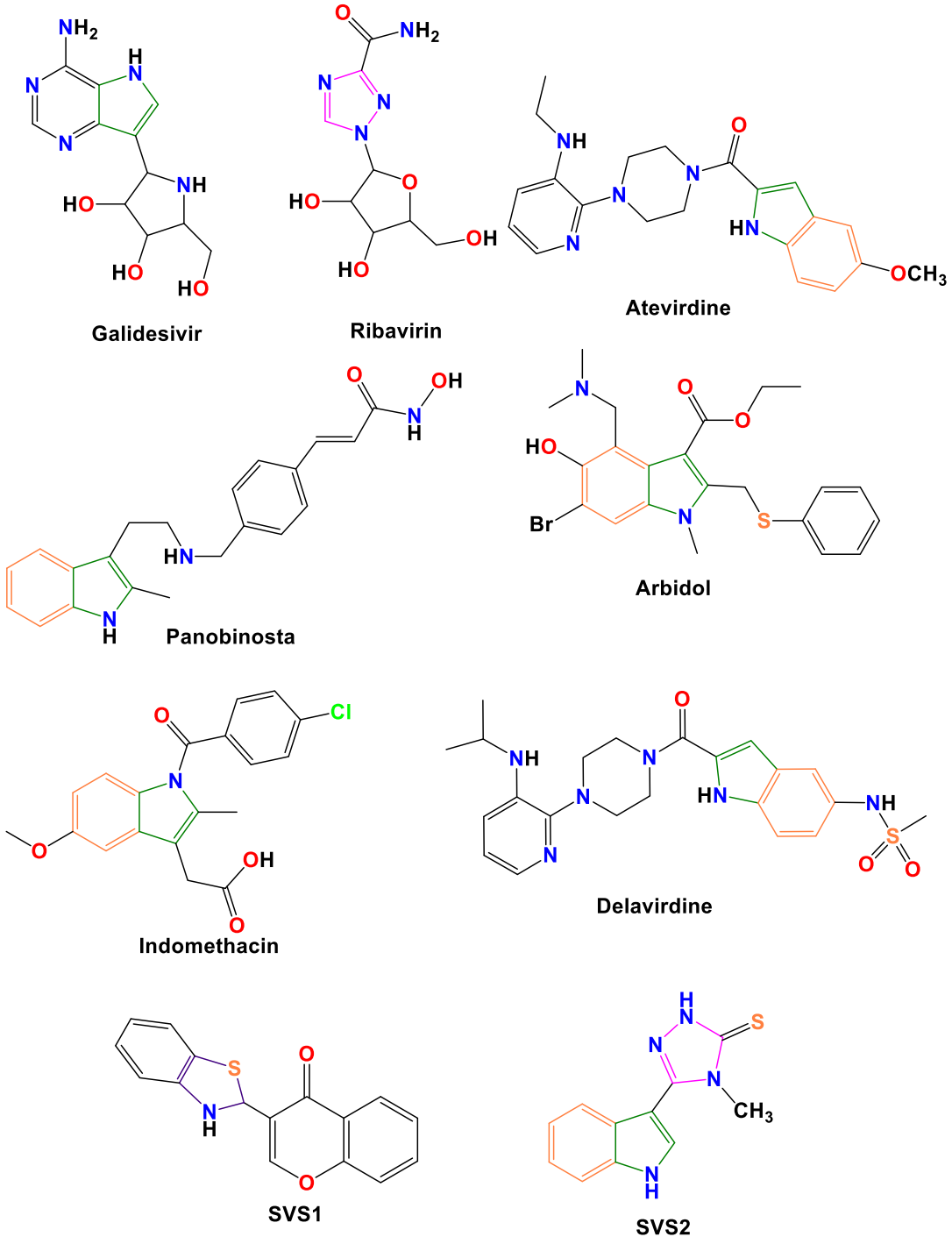

Fig. 7. Commercially available drugs containing thiazole-based heterocyclic moiety and structures of heterocyclic compounds (**SVS1** and **SVS2**) used in this work.

The gmx cluster command was used to form clusters based on the RMSD over the entire 50 ns time frame, and a representative of the largest cluster was taken as the average complex structure. It was observed the **SVS1** is found to interact in the active site pocket of the enzyme both in the initial pose and also in the average complex structure. This indicates that **SVS1** has not deviated much from the active site pocket and has been quite stable in the active site throughout the 50 ns MDS. Fig. 11(a) shows the cavity of binding site with **SVS1** from the initial pose in red and from the average representative structure of the MD run in blue. On superimposing the initial and average representative structures, an RMSD of 1.8 Å was calculated and the image can be seen in Fig. 11(b). These results highlight the stability of **SVS1** at the active site of the enzyme throughout the simulation, and it maintained the dynamic interactions at the active site of the SARS-CoV-2 main protease.

3.8. Cytotoxic ability of the compounds

Indole derivatives induce apoptosis, and inhibit proliferation, expansion and invasion of human cancer cells *via* various targets such as histone deacetylases (HDACs), sirtuins, PIM kinases, DNA topoisomerases and σ receptors [59–61]. Chromone compounds such as PD98059 and myricetin act as highly specific MEK1/2 inhibitors in hepatocarcinoma (HCC), prostate carcinoma, non-small

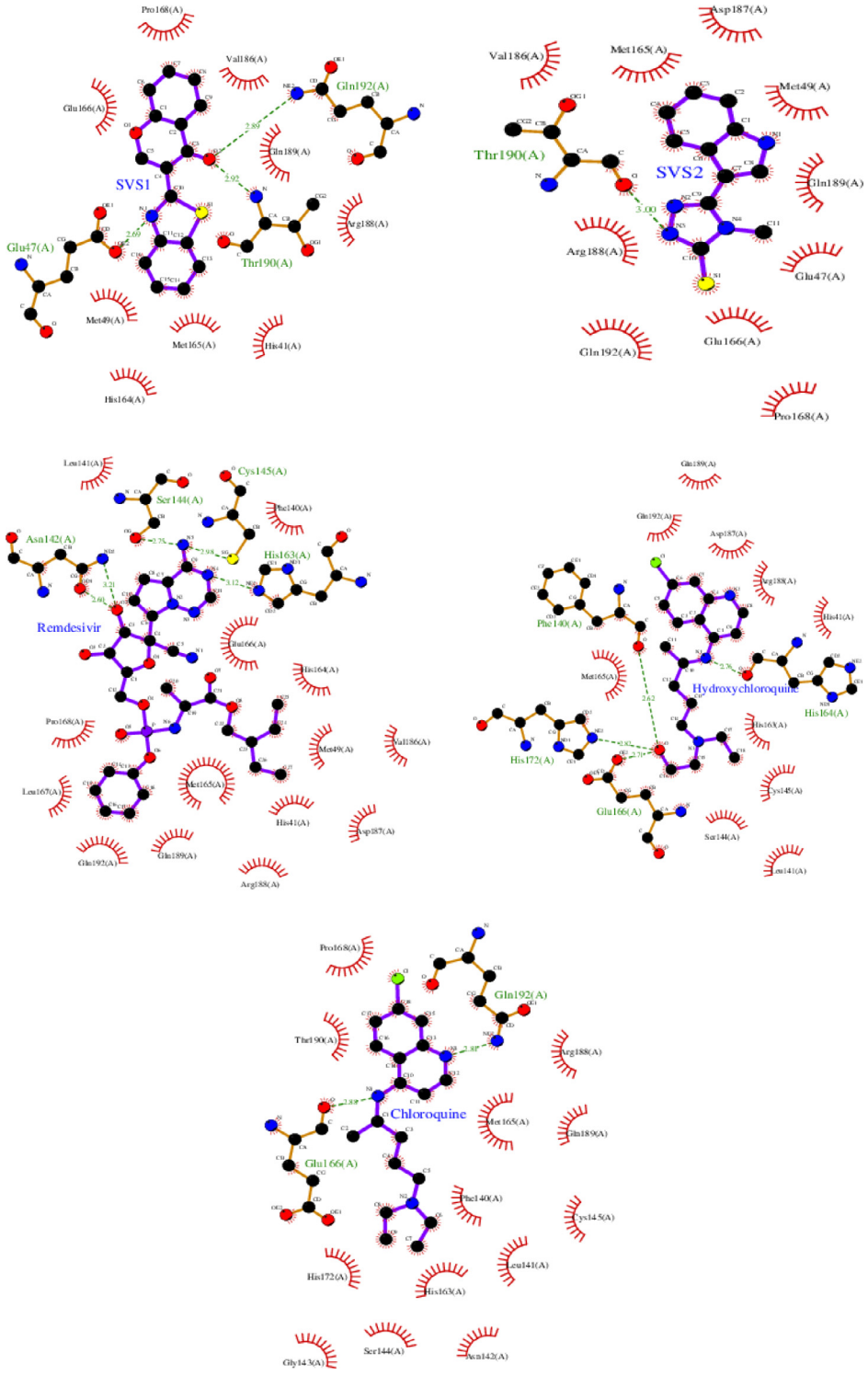

Fig. 8. Ligplot image showing the hydrogen bonds (green dashed lines) and hydrophobic interactions (red arcs) of the compounds (**SVS1**, **SVS2**, remdesivir, hydroxychloroquine and chloroquine) at the active site of SARS-CoV-2 main protease enzyme (6Y2F).

cell lung cancer (NSCLC), leukemia and melanoma [62]. Various small molecules of triazoles can specifically arrest tumor cells [16,63]. The cell viability (%) obtained after 24 h for the present compounds against HepG-2, T24 and EA.hy926 cancer cells showed growth-inhibition in a dose-dependent manner (Fig. 12a and 12b). The cell viability decreased with the increasing concentrations of **SVS1, SVS2**, cisplatin and doxorubicin. The IC_{50} values of compounds are listed in Table 7. The IC_{50} values of **SVS1, SVS2**, cisplatin and doxorubicin were >50, 33.8, 49.9 and 8.6 μM against HepG-2 cell line, >50, 29.2, 26.6 and 3.8 μM against EA.hy926 cell line, and 44.8 (**SVS1**), 46.7 (**SVS2**) and >50 μM (cisplatin) against T24 cell line, respectively. Cell proliferation assay results showed that **SVS2** possessed good cytotoxicity against HepG-2 cancer cells. The ability of **SVS1, SVS2**, cisplatin and doxorubicin to

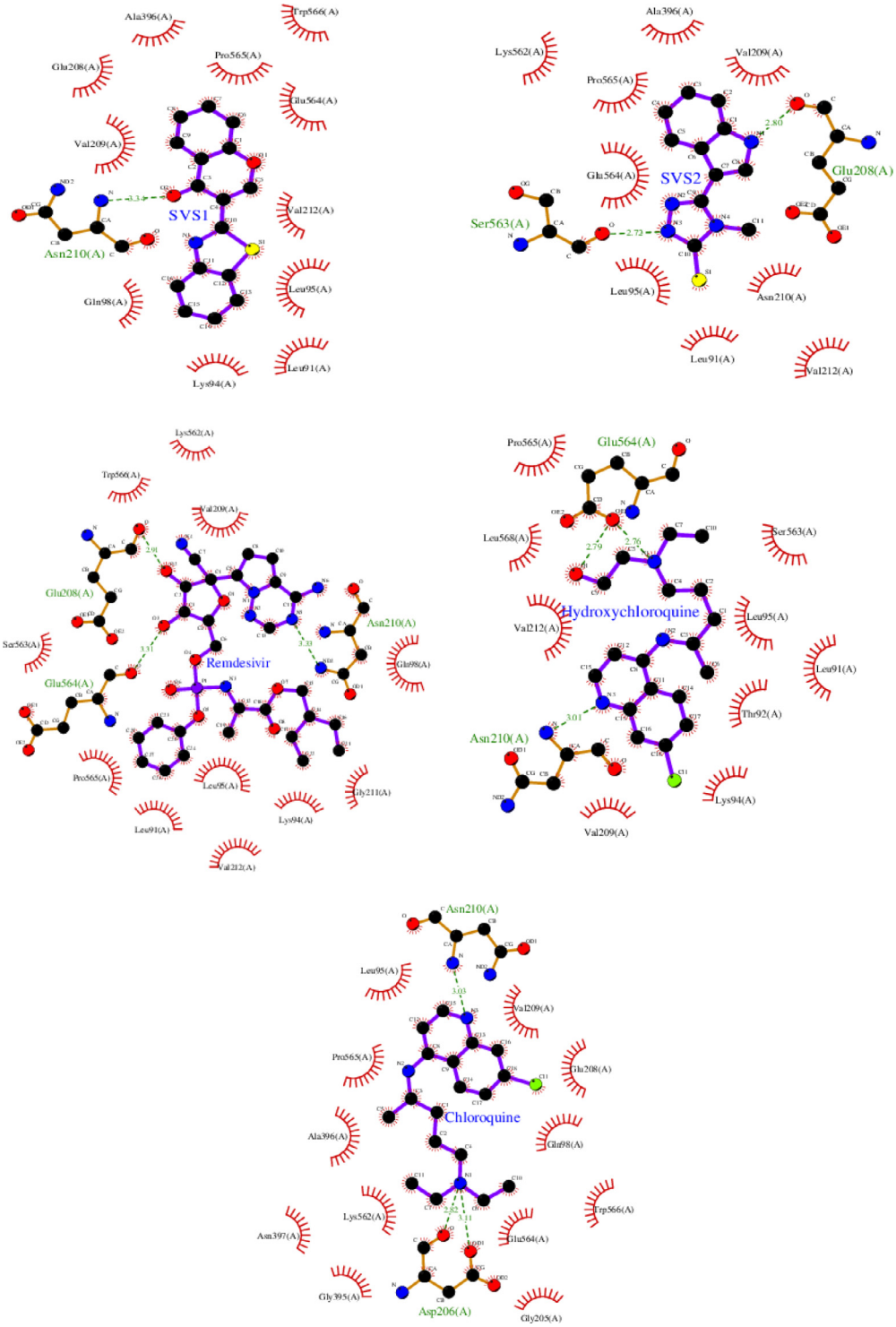

Fig. 9. Ligplot image showing the hydrogen bonds (green dashed lines) and hydrophobic interactions (red arcs) of the compounds (**SVS1**, **SVS2**, remdesivir, hydroxychloroquine and chloroquine) at the active site of human ACE-2 enzyme (6M0J).

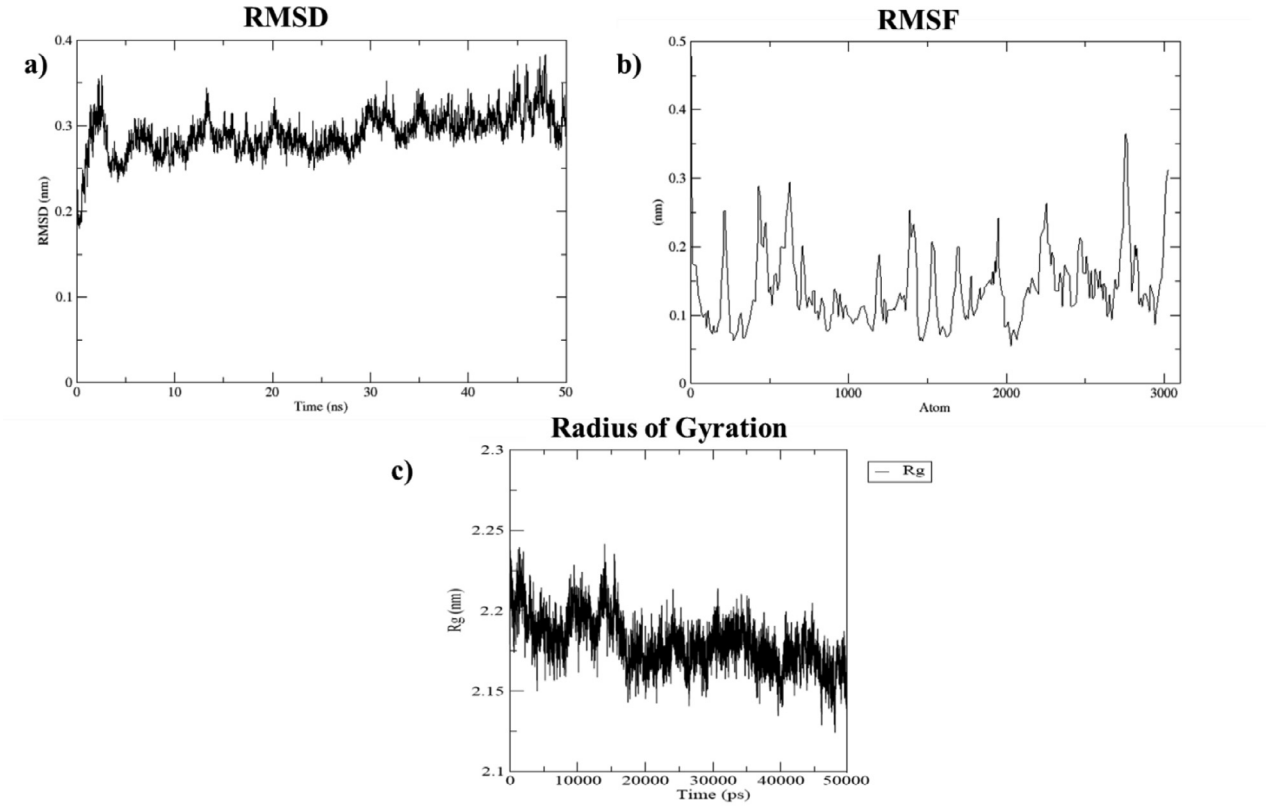

Fig. 10. a) RMSD, b) RMSF and c) Radius of gyration graphs of the SARS-CoV-2 main protease (6Y2F) with **SVS1** obtained from 50 ns molecular dynamics simulation.

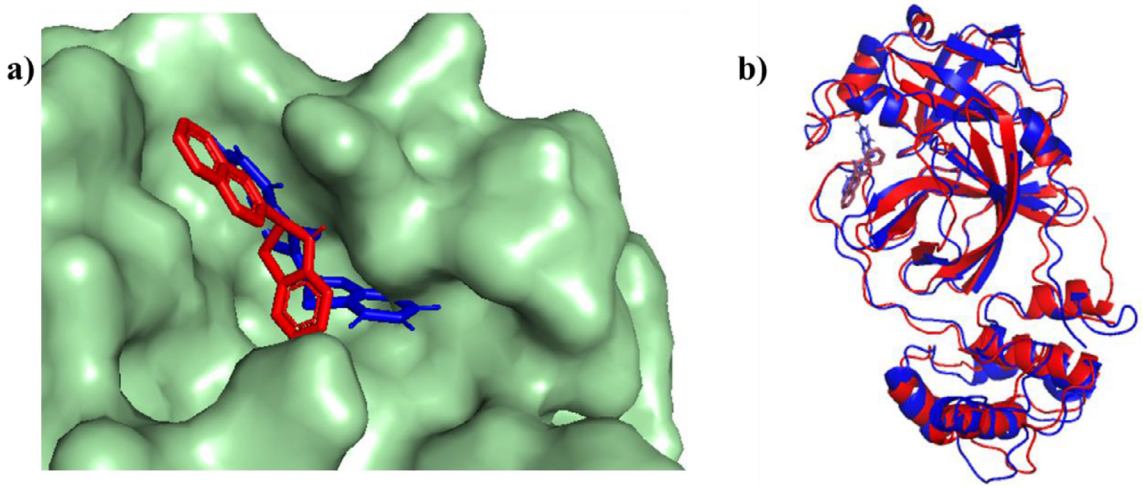

Fig. 11. a) Binding pocket showing **SVS1** in red from the initial pose and blue from the average representative structure from MDS and b) Superimposed image of the initial (red) and average representative (blue) structures of 6Y2F-**SVS1** complex (RMSD = 1.8 Å).

Table 6
Docking energies (kcal/mol) of the compounds bound at the active site of the enzymes SARS-CoV-2 main protease and human ACE-2 receptor.

Compound	Docking energy (kcal/mol)	
	SARS-CoV-2 main protease	Human ACE-2 receptor
SVS1	−7.79	−8.48
SVS2	−7.38	−7.28
Remdesivir	−7.16	−7.26
Chloroquine	−6.47	−8.23
Hydroxychloroquine	−6.68	−9.07

Table 7
Half maximal inhibitory concentration (IC_{50}) values of the compounds in HepG-2-hepatic carcinoma, T24-bladder, EA.hy926-endothelial cancer and Vero-kidney epithelial normal cells extracted from an African green monkey cell lines as calculated by MTT assay after 24 h incubation at 37 °C, 5% CO_2.

Compound	IC_{50} (μM)			
	HepG-2	T24	EA.hy926	Vero
SVS1	>50	44.8	>50	>100
SVS2	33.8	46.7	29.2	>100
Cisplatin	49.9	>50	26.6	29.5
Doxorubicin	8.6	NT	3.8	8.7

NT = Not tested.

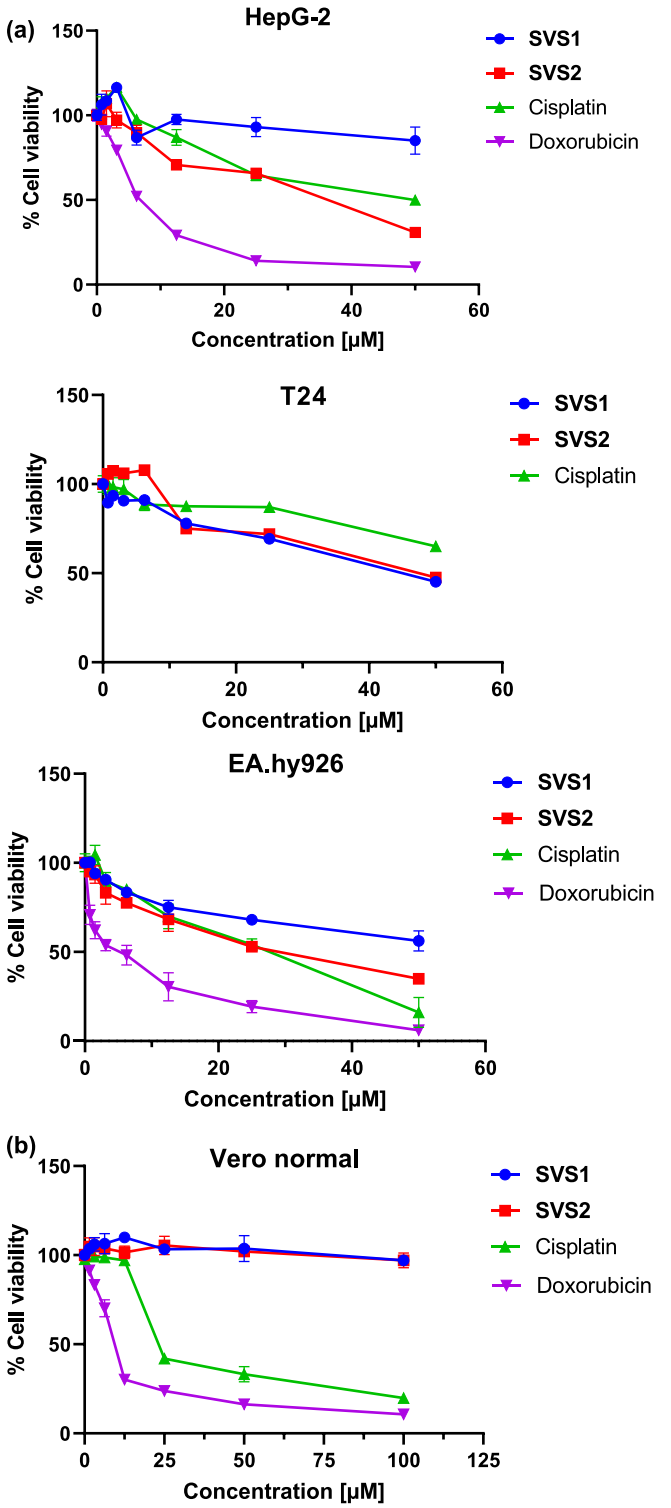

Fig. 12. a) Cytotoxicity of **SVS1**, **SVS2** and cisplatin against HepG-2, T24 and EA.hy926 cancer cells after 24 h incubation time. Each value represents the mean ± SD for $n = 3$. $p < 0.05$. b) Cytotoxicity of **SVS1, SVS2** and cisplatin against Vero normal cells after 24 h incubation time. Each value represents the mean ± SD for $n = 3$. $p < 0.05$.

kill the HepG-2 cells vary as doxorubicin > **SVS2** > cisplatin > **SVS1** at 24 h, and interestingly, **SVS2** was significantly more cytotoxic (ANOVA, $p < 0.05$) against HepG-2 cells than cisplatin and showed less activity than doxorubicin. On comparing the IC_{50} values of **SVS1, SVS2** and cisplatin (Table 7), it was found that **SVS1** and **SVS2** were more active against T24 cells than cisplatin. Further, the cytotoxicity of **SVS1** was more than that of **SVS2** against T24 cells. In addition, both **SVS2** and cisplatin were highly toxic against EA.hy926 cancer cells. To explore the selectivity, the cytotoxicity of **SVS1, SVS2** and cisplatin was investigated in Vero normal cells. The IC_{50} values of **SVS1, SVS2**, cisplatin and doxorubicin against Vero normal cells were >100, >100, 29.5 and 8.9 μM, respectively (Table 7). It appears as **SVS1** and **SVS2** were selective to cancer cell lines, and hence these can be tested as chemotherapeutic drugs.

4. Conclusions

SVS1 was prepared from 2-aminothiophenol and 4-oxo-4H-chromene-3-carbaldehyde. **SVS2** was synthesized from (*E*)−2-((1H-indol-3-yl)methylene)-N-methylhydrazine-1-carbothioamide in the presence of anhydrous $FeCl_3$. **SVS1** and **SVS2** were thioazole (with chromone) and triazole (with indole) heterocyclic compounds, respectively. They were characterized by analytical and spectroscopic methods. The solid-state structures were confirmed by single crystal X-ray diffraction technique. Quantum chemical parameters such as electronic chemical potential (μ), global hardness (η), global softness (σ), absolute electronegativity (χ) and electrophilicity index (ω) were assessed using module $DMol^3$ in Materials Studio 2017. The calculated energy gap of **SVS1** and **SVS2** showed that the chemical reactivity of **SVS1** was more than that of **SVS2**. As a result, the hardness of **SVS1** was lower than that of **SVS2**. In addition, **SVS2** had high stability and polarization. The electrons of **SVS2** might be able to be transferred to the biological systems rather than those of **SVS1** due to the high chemical potential of **SVS2.** **SVS2** possessed a high value of electrophilicity index (ω) compared to **SVS1**, which can be correlated with its high toxicity. Hence, **SVS2** can act as a better cytotoxic compound even at low concentrations. Based on quantum calculations, **SVS2** as electron acceptor, was more reactive when compared with **SVS1** due to its more negative E_{LUMO}. Binding energies of the compounds with the target enzymes based on the molecular docking results clearly showed that **SVS1** had more binding potential than **SVS2**. The active site interactions of **SVS1** and **SVS2** were comparable with remdesivir, chloroquine and hydroxychloroquine. Molecular dynamics simulation of M^{pro}–**SVS1** complex clearly showed the stability of **SVS1** to interact only at the active site of the enzyme. At last, the study was complemented by the cytotoxic activity of compounds against three human cancer (HepG-2, T24 and EA.hy926) and one normal (Vero) cells. **SVS2** was more active than the other compounds against liver (HepG-2) cancer cells. In addition, **SVS1** and **SVS2** were more active against T24-bladder cancer cells than cisplatin. Furthermore, it was found that **SVS2** and cisplatin had a higher cytotoxic activity than **SVS1** against EAhy926 cancer cells. The IC_{50} values of **SVS1, SVS2** and cisplatin against Vero normal cells showed that **SVS1** and **SVS2** were selectively toxic against the cancer cells. The mode of cell death and *in vitro* cytotoxicity will be analyzed to further establish its therapeutic potential as anticancer/antiviral agent.

Appendix A. Supplementary data

All the spectra and tables are provided. Crystallographic data for the structures reported in this paper have been deposited with the Cambridge Crystallographic Data Center (CCDC) as supplementary publication numbers (CCDC 2053105 and 2053106 for **SVS1** and **SVS2**, respectively). Copies of the data can be obtained free of charge from the CCDC (12 Union Road, Cambridge CB2 1EZ, UK; Tel.: + 44–1223–336408; Fax: + 44–1223–336003; e-mail: deposit@ccdc.cam.ac.uk; web site: http://www.ccdc.cam.ac.uk).

Declaration of Competing Interest

The authors declare that they have no known competing financial interests or personal relationships that could have appeared to influence the work reported in this paper.

CRediT authorship contribution statement

Jebiti Haribabu: Writing – original draft, Investigation, Methodology. **Vasavi Garisetti:** Software, Formal analysis, Writing – review & editing. **Rahime Eshaghi Malekshah:** Software, Formal analysis, Writing – review & editing. **Swaminathan Srividya:** Writing – original draft, Investigation, Methodology. **Dasararaju Gayathri:** Software, Formal analysis, Writing – review & editing. **Nattamai Bhuvanesh:** Software, Formal analysis, Writing – review & editing. **Ramalinga Viswanathan Mangalaraja:** Software, Formal analysis, Writing – review & editing. **Cesar Echeverria:** Writing – original draft, Investigation, Methodology, Supervision. **Ramasamy Karvembu:** Writing – original draft, Investigation, Methodology, Supervision.

Acknowledgments

J. H. thanks the Fondo Nacional de Ciencia y Tecnologia (FONDECYT, Project No. 3200391 and 11170840) for fellowship. S. S. and V. G. thanks the Department of Science and Technology, Ministry of Science and Technology, Government of India, for doctoral fellowship under the DST-INSPIRE (IF160449 and IF160596) program.

Supplementary materials

Supplementary material associated with this article can be found, in the online version, at doi:10.1016/j.molstruc.2021.131782.

References

[1] J.R. Cavalcante, A.C. Cardoso-dos-Santos, J.M. Bremm, A. de P. Lobo, E.M. Macário, W.K. de Oliveira, G.V.A. de França, COVID-19 in Brazil: evolution of the epidemic up until epidemiological week 20 of 2020, Epidemiol. Serv. Saude 29 (2020) e2020376.
[2] J. Haribabu, S. Srividya, D. Mahendiran, D. Gayathri, V. Venkatramu, N. Bhuvanesh, R. Karvembu, Synthesis of palladium(II) complexes *via* Michael addition: antiproliferative effects through ROS-mediated mitochondrial apoptosis and docking with SARS-CoV-2, Inorg. Chem. 59 (2020) 17109–17122.
[3] M. Venkateshan, M. Muthu, J. Suresh, R.R. Kumar, Azafluorene derivatives as inhibitors of SARS-CoV-2 RdRp: synthesis, physicochemical, quantum chemical, modeling and molecular docking analysis, J. Mol. Struct. 1220 (2020) 128741.
[4] U. De S Senapathi, M. Aboelkhair, K. Puro, M. Ali, A. Amarasinghe, M.S. Abdul-Cader, G. Van Marle, M. Czub, M.F. Abdul-Careem, In Ovo delivered toll–like receptor 7 ligand, resiquimod enhances host responses against infectious bronchitis corona virus (IBV) infection, Vaccines 8 (2020) 186 (Basel).
[5] S. Pant, M. Singh, V. Ravichandiran, U.S.N. Murty, H.K. Srivastava, Peptide–like and small-molecule inhibitors against Covid-19, J. Biomol. Struct. Dyn. 39 (2020) 2904–2913.
[6] A.K. Srivastava, A. Kumar, N. Misra, P.S. Manjula, B.K. Sarojini, B. Narayana, Synthesis, spectral (FT-IR, UV-visible, NMR) features, biological activity prediction and theoretical studies of 4-amino-3-(4-hydroxybenzyl)-1H-1,2,4-triazole-5(4H)-thione and its tautomer, J. Mol. Struct. 1107 (2016) 137–144.
[7] P.E. Larchanche, V. Ultré, D. Le Broc, C. Ballandone, C. Furman, P. Dallemagne, P. Melnyk, P. Carato, 6-Sulfonylbenzothiazolones as potential scaffolds for the design of 5- HT6 ligands, Eur. J. Med. Chem. 92 (2015) 807–817.
[8] H.A.M. El-Sherief, B.G.M. Youssif, S.N. Abbas Bukhari, A.H. Abdelazeem, M. Abdel-Aziz, H.M. Abdel-Rahman, Synthesis, anticancer activity and molecular modeling studies of 1,2,4-triazole derivatives as EGFR inhibitors, Eur. J. Med. Chem. 156 (2018) 774–789.
[9] J. Haribabu, G.R. Subhashree, S. Saranya, K. Gomathi, R. Karvembu, D. Gayathri, Synthesis, crystal structure, and *in vitro* and *in silico* molecular docking of novel acyl thiourea derivatives, J. Mol. Struct. 1094 (2015) 281–291.
[10] J. Haribabu, G.R. Subhashree, S. Saranya, K. Gomathi, R. Karvembu, D. Gayathri, Isatin based thiosemicarbazone derivatives as potential bioactive agents: anti-oxidant and molecular docking studies, J. Mol. Struct. 1110 (2016) 185–195.
[11] L. Labanauskas, E. Udrenaite, P. Gaidelis, A. Brukštus, Synthesis of 5-(2-,3- and 4-methoxyphenyl)-4H-1,2,4-triazole-3-thiol derivatives exhibiting anti-inflammatory activity, Farmaco 59 (2004) 255–259.
[12] T. Plech, M. Wujec, U. Kosikowska, A. Malm, B. Rajtar, M. Polz-Dacewicz, Synthesis and *in vitro* activity of 1,2,4-triazole-ciprofloxacin hybrids against drug–susceptible and drug-resistant bacteria, Eur. J. Med. Chem. 60 (2013) 128–134.
[13] S.K.J. Shaikh, R.R. Kamble, P.K. Bayannavar, S.M. Somagond, S.D. Joshi, Triazolothiadizepinylquinolines as potential MetAP-2 and NMT inhibitors: microwave-assisted synthesis, pharmacological evaluation and molecular docking studies, J. Mol. Struct. 1203 (2020) 127445.
[14] U. Salgın-Gökşen, N. Gökhan-Kelekçi, Ö. Göktaş, Y. Köysal, E. Kılıç, Ş. Işık, G. Aktay, M. Özalp, 1-Acylthiosemicarbazides, 1,2,4-triazole-5(4H)-thiones, 1,3,4-thiadiazoles and hydrazones containing 5-methyl-2-benzoxazolinones: synthesis, analgesic-anti-inflammatory and antimicrobial activities, Bioorg. Med. Chem. 15 (2007) 5738–5751.
[15] T. Plech, B. Kaproń, J.J. Łuszczki, A. Paneth, A. Siwek, M. Kołaczkowski, M. Żołnierek, G. Nowak, Studies on the anticonvulsant activity of 4-alkyl-1,2,4-triazole-3-thiones and their effect on GABAergic system, Eur. J. Med. Chem. 86 (2014) 690–699.
[16] S.G. Küçükgüzel, P. Çıkla-Süzgün, Recent advances bioactive 1, 2, 4-triazole-3-thiones, Eur. J. Med. Chem. 97 (2015) 830–870.
[17] J. Luszczki, E. Marzeda, M.W. Kondrat-Wrobel, D. Pyrka, S.L. Kocharov, M. Florek-Luszczki, Effect of N-(m-bromoanilinomethyl)-*p*-isopropoxyphenylsuccinimide on the anticonvulsant action of four classical antiepileptic drugs in the mouse maximal electroshock-induced seizure model, Curr. Issues Pharm. Med. Sci. 27 (2014) 76–79.
[18] W.M. Xu, S.Z. Li, M. He, S. Yang, X.Y. Li, P. Li, Synthesis and bioactivities of novel thioether/sulfone derivatives containing 1,2,3-thiadiazole and 1,3,4-oxadiazole/thiadiazole moiety, Bioorg. Med. Chem. Lett. 23 (2013) 5821–5824.
[19] A. Demirbas, D. Sahin, N. Demirbas, S.A. Karaoglu, Synthesis of some new 1,3,4-thiadiazol-2-ylmethyl-1,2,4-triazole derivatives and investigation of their antimicrobial activities, Eur. J. Med. Chem. 44 (2009) 2896–2903.
[20] İ. Timur, Ü.M. Kocyigit, T. Dastan, S. Sandal, A.O. Ceribası, P. Taslimi, İ. Gulcin, M. Koparir, M. Karatepe, M. Çiftçi, *In vitro* cytotoxic and *in vivo* antitumoral activities of some aminomethyl derivatives of 2,4-dihydro-3H-1,2,4-triazole-3-thiones - evaluation of their acetylcholinesterase and carbonic anhydrase enzymes inhibition profiles, J. Biochem. Mol. Toxicol. 33 (2019) e22239.
[21] Z. Song, Y. Zhou, W. Zhang, L. Zhan, Y. Yu, Y. Chen, W. Jia, Z. Liu, J. Qian, Y. Zhang, C. Li, G. Liang, Base promoted synthesis of novel indole-dithiocarbamate compounds as potential anti-inflammatory therapeutic agents for treatment of acute lung injury, Eur. J. Med. Chem. 171 (2019) 54–65.
[22] N. Karal, A. Gürsoy, F. Kandemirli, N. Shvets, F.B. Kaynak, S. Özbey, V. Kovalishyne, A. Dimogloc, Synthesis and structure-antituberculosis activity relationship of 1H-indole-2,3-dione derivatives, Bioorg. Med. Chem. 15 (2007) 5888–5904.
[23] C.K. Ryu, J.Y. Lee, R.E. Park, M.Y. Ma, J.H. Nho, Synthesis and antifungal activity of 1H-indole-4,7-diones, Bioorg. Med. Chem. Lett. 17 (2007) 127–131.
[24] Y. Chang, J. Zhang, S.S. Yang, W. Lu, L. Ding, Y. Zheng, W. Li, Design, synthesis, biological evaluation, and molecular docking of 1,7-dibenzyl-substituted theophylline derivatives as novel BRD4-BD1-selective inhibitors, Med. Chem. Res. 30 (2021) 1453–1468.
[25] K. Kanagasabai, P. Mariappan, P. Ragunathan, H. Balasubramanian, H. Arumugasamy, Synthesis, anticancer and antioxidant activities of 7-methoxyisoflavanone and 2,3-diarylchromanones, Eur. J. Med. Chem. 45 (2010) 2447–2452.
[26] J. Haribabu, C. Balachandran, M.M. Tamizh, Y. Arun, N.S.P. Bhuvanesh, S. Aoki, R. Karvembu, Unprecedented formation of palladium(II)-pyrazole based thiourea from chromone thiosemicarbazone and $[PdCl_2(PPh_3)_2]$: interaction with biomolecules and apoptosis through mitochondrial signaling pathway, J. Inorg. Biochem. 205 (2020) 110988.
[27] C.W. Robinson, C.S. Rye, N.E.A. Chessum, K. Jones, A model β-sheet interaction and thermodynamic analysis of β-strand mimetics, Org. Biomol. Chem. 13 (2015) 7402–7407.
[28] L.G. Meng, H.F. Liu, J.L. Wei, S.N. Gong, S. Xue, One-pot reaction of ortho-acylphenols and terminal alkynoates for synthesis of 2-alkyl-substituted chromanones, Tetrahedron Lett. 51 (2010) 1748–1750.
[29] N. Murugesh, J. Haribabu, K. Arumugam, C. Balachandran, R. Swaathy, S. Aoki, A. Sreekanth, R. Karvembu, S. Vedachalam, NHC-catalyzed green synthesis of functionalized chromones: DFT mechanistic insights and *in vitro* activities in cancer cells, New J. Chem. 43 (2019) 13509–13525.
[30] J. Reis, F. Cagide, D. Chavarria, T. Silva, C. Fernandes, A. Gaspar, E. Uriarte, F. Remião, S. Alcaro, F. Ortuso, F. Borges, Discovery of new chemical entities for old targets: insights on the lead optimization of chromone-based monoamine oxidase B (MAO-B) inhibitors, J. Med. Chem. 59 (2019) 5879–5893.
[31] J. Nawrot-Modranka, E. Nawrot, J. Graczyk, *In vivo* antitumor, *in vitro* antibacterial activity and alkylating properties of phosphorohydrazine derivatives of coumarin and chromone, Eur. J. Med. Chem. 41 (2006) 1301–1309.
[32] W. Sun, P.J. Carroll, D.R. Soprano, D.J. Canney, Identification of a chromone-based retinoid containing a polyolefinic side chain *via* facile synthetic routes, Bioorg. Med. Chem. Lett. 19 (2009) 4339–4342.
[33] H. Cho, S.H. Seo, Y. Na, Y. Kwon, The synthesis and anticancer activities of chiral epoxy-substituted chromone analogs, Bioorg. Chem. 84 (2019) 347–354.
[34] J. Haribabu, G. Sabapathi, M.M. Tamizh, C. Balachandran, N.S.P. Bhuvanesh, P. Venuvanalingam, R. Karvembu, Water-soluble mono- and binuclear Ru(η^6-*p*-cymene) complexes containing indole thiosemicarbazones: synthesis, DFT modeling, biomolecular interactions, and *in vitro* anticancer activity through apoptosis, Organometallics 37 (2018) 1242–1257.

[35] N. Balakrishnan, J. Haribabu, D.A. Krishnan, S. Swaminathan, D. Mahendiran, N.S.P. Bhuvanesh, R. Karvembu, Zinc(II) complexes of indole thiosemicarbazones: DNA/protein binding, molecular docking and *in vitro* cytotoxicity studies, Polyhedron 170 (2019) 188–201.
[36] J. Haribabu, K. Jeyalakshmi, Y. Arun, N.S.P. Bhuvanesh, P.T. Perumal, R. Karvembu, Synthesis of Ni(II) complexes bearing indole-based thiosemicarbazone ligands for interaction with biomolecules and some biological applications, J. Biol. Inorg. Chem. 22 (2017) 461–480.
[37] G.M. Sheldrick, A short history of SHELX, Acta Crystallogr. Sect. A Found. Crystallogr. 64 (2008) 112–122.
[38] G.M. Sheldrick, Crystal structure refinement with SHELXL, Acta Crystallogr. Sect. C Struct. Chem. 71 (2015) 3–8.
[39] O.V. Dolomanov, L.J. Bourhis, R.J. Gildea, J.A.K. Howard, H. Puschmann, Olex2: a complete structure solution, refinement and analysis program, J. Appl. Crystallogr. 42 (2009) 339–341.
[40] R. Pelalak, R. Soltani, Z. Heidari, R.E. Malekshah, M. Aallaei, A. Marjani, M. Rezakazemi, T.A. Kurniawan, S. Shirazian, Molecular dynamics simulation of novel diamino-functionalized hollow mesosilica spheres for adsorption of dyes from synthetic waste water, J. Mol. Liq. 322 (2021) 114812.
[41] G.M. Morris, R. Huey, W. Lindstrom, M.F. Sanner, R.K. Belew, D.S. Goodsell, A.J. Olson, AutoDock4 and AutoDockTools4: automated docking with selective receptor flexibility, J. Comp. Chem. 30 (16) (2009) 2785–2791.
[42] R.A. Laskowski, M.B. Swindells, LigPlot+: multiple ligand-protein interaction diagrams for drug discovery, J. Chem. Inf. Model. 51 (2011) 2778–2786.
[43] M.J. Abraham, T. Murtola, R. Schulzb, S. Pálla, J.C. Smith, B. Hess, E. Lindahl, GROMACS: high performance molecular simulations through multi-level parallelism from laptops to supercomputers, SoftwareX 1-2 (2015) 19–25.
[44] H.G. Petersen, Accuracy and efficiency of the particle mesh Ewald method, J. Chem. Phys. 103 (1995) 3668–3679.
[45] L. Schrödinger, W. DeLano. PyMOL, 2020. http://www.pymol.org/pymol.
[46] J. Haribabu, O.I. Alajrawy, K. Jeyalakshmi, C. Balachandran, D.A. Krishnan, N. Bhuvanesh, S. Aoki, K. Natarajan, R. Karvembu, N-substitution in isatin thiosemicarbazones decides nuclearity of Cu(II) complexes – spectroscopic, molecular docking and cytotoxic studies, Spectrochim. Acta A Mol. Biomol. Spectrosc. 246 (2021) 118963.
[47] J. Haribabu, M.M. Tamizh, C. Balachandran, Y. Arun, N.S.P. Bhuvanesh, A. Endo, R. Karvembu, Synthesis, structures and mechanistic pathways of anticancer activity of palladium(II) complexes with indole-3-carbaldehyde thiosemicarbazones, New J. Chem. 42 (2018) 10818–10832.
[48] C. Balachandrana, J. Haribabu, K. Jeyalakshmi, N.S.P. Bhuvanesh, R. Karvembu, N. Emi, S. Awale, Nickel(II) bis(isatin thiosemicarbazone) complexes induced apoptosis through mitochondrial signaling pathway and G0/G1 cell cycle arrest in IM-9 cells, J. Inorg. Biochem. 182 (2018) 208–221.
[49] A. Guediri, A. Bouguettoucha, D. Chebli, N. Chafai, A. Amrane, Molecular dynamic simulation and DFT computational studies on the adsorption performances of methylene blue in aqueous solutions by orange peel-modified phosphoric acid, J. Mol. Struct. 1202 (2020) 127290.
[50] F. Sama, M. Raizada, M. Ashafaq, M.N. Ahamad, I. Mantasha, K. Iman, M.S. Rahisuddin, R. Arif, N.A. Shah, H.A.M. Saleh, Synthesis, structure and DNA binding properties of a homodinuclear Cu(II) complex: an experimental and theoretical approach, J. Mol. Struct. 1176 (2019) 283–289.
[51] M. Venkateshan, J. Suresh, Synthesis, physicochemical and quantum chemical studies on a new organic NLO crystal: cinnamoylproline, J. Mol. Struct. 1180 (2019) 826–838.
[52] V.R. Mishra, C.W. Ghanavatkar, S.N. Mali, H.K. Chaudhari, N. Sekar, Schiff base clubbed benzothiazole: synthesis, potent antimicrobial and MCF-7 anticancer activity, DNA cleavage and computational study, J. Biomol. Struct. Dyn. 38 (2020) 1772–1785.
[53] T. Madanhire, H. Davids, M.C. Pereira, E.C. Hosten, A. Abrahams, Synthesis, characterisation and anticancer activity screening of lanthanide(III) acetate complexes with benzohydrazone and nicotinohydrazone ligands, Polyhedron 184 (2020) 114560.
[54] S. Karthikeyan, G. Bharanidharan, R. Mangaiyarkarasi, S. Chinnathambi, R. Sriram, K. Gunasekaran, K. Saravanan, M. Gopikrishnan, P. Aruna, S. Ganesan, A cytotoxicity, optical spectroscopy and computational binding analysis of 4-[3-acetyl-5-(acetylamino)-2-methyl-2,3-dihydro-1,3,4-thiadiazole-2-yl]phenyl benzoate in calf thymus DNA, Luminescence 33 (2018) 731–741.
[55] A.G. Trindade, S.M.C. Caxito, A.R.E.O. Xavier, M.A.S. Xavier, F. Brandão, COVID-19: therapeutic approaches description and discussion, An. Acad. Bras. Cienc. 92 (2020) 1–15.
[56] M.A. Mansour, A.M. Aboulmagd, H.M. Abdel-Rahman, Quinazoline-Schiff base conjugates: *in silico* study and ADMET predictions as multi-target inhibitors of coronavirus (SARS-CoV-2) proteins, RSC Adv. 10 (2020) 34033–34045.
[57] D.A. Milenković, D.S. Dimić, E.H. Avdović, Z.S. Marković, Several coumarin derivatives and their Pd(II) complexes as potential inhibitors of the main protease of SARS-CoV-2, an *in silico* approach, RSC Adv. 10 (2020) 35099–35108.
[58] S. Ullrich, C. Nitsche, The SARS-CoV-2 main protease as drug target, Bioorg. Med. Chem. Lett. 30 (2020) 127377.
[59] C.G. Neochoritis, A. Dömling, Towards a facile and convenient synthesis of highly functionalized indole derivatives based on multi-component reactions, Org. Biomol. Chem. 12 (10) (2014) 1649–1651.
[60] N.K. Kaushik, N. Kaushik, P. Attri, N. Kumar, C. Hyeok Kim, A.K. Verma, E. Ha Choi, Biomedical importance of indoles, Molecules 18 (2013) 6620–6662.
[61] S. Dadashpour, S. Emami, Indole in the target-based design of anticancer agents: a versatile scaffold with diverse mechanisms, Eur. J. Med. Chem. 150 (2018) 9–29.
[62] H. Chen, C. Qiao, T.T. Miao, A.L. Li, W.Y. Wang, W. Gu, Synthesis and biological evaluation of novel N-(piperazin-1-yl)alkyl-1H-dibenzo[a,c]carbazole derivatives of dehydroabietic acid as potential MEK inhibitors, J. Enzyme Inhib. Med. Chem. 34 (2019) 1544–1561.
[63] J.K. Shneine, Y.H. Alaraji, Chemistry of 1,2,4-triazole: a review article, Int. J. Sci. Res. 5 (2016) 1411–1423.